

# The VISTA Orion mini-survey: star formation in the Lynds 1630 North cloud ★

L. Spezzi<sup>1,2</sup>, M. G. Petr-Gotzens<sup>1</sup>, J. M. Alcalá<sup>3</sup>, J. K. Jørgensen<sup>4</sup>, T. Stanke<sup>1</sup>, M. Lombardi<sup>5,6</sup>, J. F. Alves<sup>7</sup>

<sup>1</sup> European Southern Observatory, Karl-Schwarzschild-Straße 2, 85748 Garching bei München, Germany e-mail: loredana.spezzi@gmail.com

<sup>2</sup> European Organisation for the Exploitation of Meteorological Satellites (EUMETSAT), Eumetsat Allee 1, 64295 Darmstadt, Germany

<sup>3</sup> INAF - Osservatorio Astronomico di Capodimonte, via Moiariello, 16, 80131 Napoli, Italy

<sup>4</sup> Niels Bohr Institute, University of Copenhagen, Juliane Maries Vej 30, DK-2100 Copenhagen Ø, Denmark

<sup>5</sup> University of Milan, Department of Physics, via Celoria 16, 20133 Milan, Italy

<sup>6</sup> Harvard-Smithsonian Center for Astrophysics, Mail Stop 72, 60 Garden Street, Cambridge, MA 02138, USA

<sup>7</sup> Institute for Astronomy, University of Vienna, Türkenschanzstr. 17, A-1180 Vienna, Austria

Received ...; accepted ...

## ABSTRACT

The Orion cloud complex presents a variety of star formation mechanisms and properties and it is still one of the most intriguing targets for star formation studies. We present VISTA/VIRCAM near-infrared observations of the L1630N star forming region, including the stellar clusters NGC 2068 and NGC 2071, in the Orion molecular cloud B and discuss them in combination with Spitzer data. We select 186 young stellar object (YSO) candidates in the region on the basis of multi-colour criteria, confirm the YSO nature of the majority of them using published spectroscopy from the literature, and use this sample to investigate the overall star formation properties in L1630N. The K-band luminosity function of L1630N is remarkably similar to that of the Trapezium cluster, i.e., it presents a broad peak in the range 0.3-0.7  $M_{\odot}$  and a fraction of sub-stellar objects of  $\sim 20\%$ . The fraction of YSOs still surrounded by disk/envelopes is very high ( $\sim 85\%$ ) compared to other star forming regions of similar age (1-2 Myr), but includes some uncertain corrections for diskless YSOs. Yet, a possibly high disk fraction together with the fact that 1/3 of the cloud mass has a gas surface density above the threshold for star formation ( $\sim 129 M_{\odot} \text{ pc}^{-2}$ ), points towards a still on-going star formation activity in L1630N. The star formation efficiency (SFE), star formation rate (SFR) and density of star formation of L1630N are within the ranges estimated for galactic star forming regions by the Spitzer "core to disk" and "Gould's Belt" surveys. However, the SFE and SFR are lower than the average value measured in the Orion A cloud and, in particular, lower than that in the southern regions of L1630. This might suggest different star formation mechanisms within the L1630 cloud complex.

**Key words.** infrared: stars – stars: pre-main sequence – Protoplanetary disks – ISM: clouds, ISM: individual objects: Orion, L1630 N – instrumentation: VISTA

## 1. Introduction

Observations of young stellar populations in nearby star forming regions are important tools to understand the interplay between the outcome of the star formation process and the original environment from which the stellar ensembles emerged. While details of the star formation process and its physics are often tested with targeted investigations on small spatial scales, global properties are best assessed with wide-field imaging surveys in the infrared thereby accomplishing large-scale studies in a homogeneous way.

The *Spitzer* c2d (Evans et al., 2009) and *Spitzer* Gould Belt (GB)<sup>1</sup> Legacy surveys (e.g., Spezzi et al., 2011; Hatchell et al., 2012; Dunham et al., 2013) effectively traced the population of young stellar objects (YSOs) in several nearby star forming regions. These studies have shown that current star-formation efficiencies are in the range from 3% to 6%, and that star formation is highly concentrated to regions of high extinction with the

youngest objects being strongly associated with dense cores. The great majority (90%) of the young stars lie within loose clusters with at least 35 members and a stellar density of  $1 M_{\odot} \text{ pc}^{-3}$  (Evans et al., 2009, and references therein). The c2d and GB surveys have also shown that the star-formation surface density in galactic star forming regions is more than an order of magnitude larger than predicted from extragalactic star formation rate – gas relationships, e.g. the Kennicutt-Schmidt law (Evans et al., 2009; Heiderman et al., 2010).

Among the most-studied nearby active star formation sites are the Orion A and Orion B molecular clouds. The clouds have similar masses of a few  $10^4 M_{\odot}$  and appear physically connected, indicating that they stem from the same overall giant molecular cloud complex. However, star formation differs quite significantly between the clouds. In Orion B almost all stars ( $\sim 90\%$ ) formed in stellar clusters (Lada et al. 1991), which concentrate at two major sites, one in the southern part of the Orion B cloud where the clusters NGC2024/23 are located and one in the northern part of Orion B (also named L1630N) with the clusters NGC2068/71. Orion A, on the other hand, shows a substantial population of distributed star formation with  $\sim 70\%$  of the stars forming in isolation (Strom et al. 1993, Fang et al.

Send offprint requests to: mpetr@eso.org

\* Based on observations collected at the ESO La Silla Paranal Observatory under programme ID 060.A-9285(B)

<sup>1</sup> <http://www.cfa.harvard.edu/gouldbelt>

2009), with the exception of the Orion Nebula Cluster which lies at the northernmost end of Orion A. Orion B contains several early B-type stars and at least one O star, while Orion A (excluding the ONC) possibly has no stars earlier than B4 and is apparently deficient in early type massive stars when compared to its known numbers of low-mass stars (Hsu et al., 2012). Furthermore, large-scale molecular gas maps indicate clear substructure on scales  $<2$  pc in Orion A, whereas Orion B displays very little substructure, although highly filamentary molecular gas seems associated with the star forming regions in the northern part of Orion B, i.e. in L1630 N (Gibb, 2008, and references therein).

In this paper we present multi-band wide-field near-infrared observations obtained with VISTA/VIRCAM, combined with mid-infrared data from Spitzer, covering approximately 1.6 square degrees in the northern part of the Orion molecular cloud B, i.e. in L1630 N

The L1630 N region contains the prominent bright optical reflection nebulosities NGC 2068 and NGC 2071 which, observed at near-infrared wavelengths, reveal their full nature as young stellar clusters. Flaherty & Muzerolle (2008) determined the clusters' age as 1-2 Myr, depending on the models used, and confirmed 67 stellar members through optical spectroscopy. However, the use of optical spectroscopy, combined with 2MASS photometry, limited their study to the least embedded and slightly higher mass objects. Fang et al. (2009) performed also optical spectroscopy of 132 stars in the region. This latter sample includes all the stars previously characterized by Flaherty & Muzerolle (2008) and several additional objects classified as Pre-Main Sequence (PMS) stars by Fang et al. (2009). These authors find a much higher disk frequency in L1630 N in comparison with L1641 (Orion A) and with other star forming regions of similar age like Chamaeleon I and IC 348, but they also caution that the results are upper limits as their sample is biased against non-disk bearing young stars. A recent study by Hsu et al. (2012) employed a photometric and spectroscopic survey to enlarge the population of confirmed members in L1641 and find the disk frequency similarly high as for L1630. Clearly, the physical characterisation of young star properties gets better defined as our census of the young star populations becomes complete.

The combination of wide field coverage and excellent sensitivity of our survey enables us to uncover a large young stellar object (YSO) population in L1630 N, which increases the number of previously known YSOs by a factor 1.5, and thereby allows us to analyse the global star formation properties in this region.

After the description of the VISTA-Orion catalog and the extraction of the data for this work in Sect. 2, we present in Sect. 3 the selection procedure of the YSO candidates in L1630 N. Then, in Sect. 4 and 5 we investigate the K-band luminosity function, initial mass function and proto-planetary disk fraction for the identified sample of YSO candidate members in L1630 N, as well as compare our results to other nearby young stellar clusters and associations. We study the spatial distribution and clustering properties of YSOs and independently confirm the known stellar clusters NGC 2068 and NGC 2071, but also identify a new stellar group around the Herbig-Haro objects HH24-26 (Sect. 6). In combination with an extinction map, derived from the same VISTA data, we also present the results on the global properties of star formation in the region and in the identified sub-structures (Sect. 7). Our conclusions are presented in Sect. 8.

**Table 1.** Filter central wavelength, saturation limit, limiting magnitude at the  $5\sigma$  level and completeness limit for the photometry of sources in tile no. 12 (L1630 N).

Filter	$\lambda_c$ ( $\mu\text{m}$ )	Saturation limit	Mag $_{5\sigma}$	Completeness limit
Z	0.877	13.5	22.5	22.3
Y	1.020	12.0	21.1	21.5
J	1.252	11.0	20.3	20.5
H	1.645	11.0	19.3	19.5
K <sub>S</sub>	2.147	10.0	18.5	18.5

## 2. Observations and data reduction

### 2.1. VISTA data reduction and catalog extraction

The Visible and Infrared Survey Telescope for Astronomy (VISTA) located at ESO Paranal Observatory is a 4m class telescope equipped with a near-IR camera (VIRCAM) containing 16 detectors, for a total FoV of  $1^\circ \times 1.5^\circ$  and a pixel scale of  $0.339''/\text{pix}$ , and available broad and narrow band filters in the wavelength range  $0.9\text{--}2.2\mu\text{m}$  (Emerson et al., 2006; Dalton et al., 2006). Data for L1630 N were taken during the VISTA Science Verification (SV) as part of the program “VISTA SV Galactic Mini-survey in Orion” (PI: M. Petr-Gotzens; Petr-Gotzens et al., 2011). This survey consists of *ZYJHK<sub>S</sub>* images obtained during 14 nights between 16 October and 2 November 2009. The survey area is a mosaic of 20 VISTA fields with each field containing 6 pointings that are mosaicked together to form a so-called filled tile. The total survey covers  $\sim 30$  square degrees around the Orion Belt stars. L1630 N is located in the VISTA Orion survey tile no. 12 roughly centered at R.A.= $05^h46^m41^s$ , Dec.= $+00^\circ09'00''$  (Figure 1), and contains the young stellar clusters NGC 2068 and NGC 2071 which clearly stand out on the VISTA near-infrared image (Figure 2). Further details on the observing strategy, the exposure times per filter and particular observing patterns chosen for the VISTA Mini-survey in Orion were described in Arnaboldi et al. (2010) and Petr-Gotzens et al. (2011).

The data reduction was performed by a dedicated pipeline, developed within the VISTA Data Flow System (VDFS), and run by the Cambridge Astronomy Survey Unit (CASU)<sup>2</sup>. The pipeline delivers science-ready stacked images and tiles, as well as photometrically and astrometrically calibrated source catalogues (Irwin et al., 2004). A total of  $\sim 3.2$  million sources were detected in the VISTA Orion Survey, and  $\sim 155000$  in tile no. 12 used for this work. The catalog also provides, for each source in each filter, a morphological parameter (FLAG) equal to  $-1$  for point-like sources,  $1$  for extended sources,  $-2$  for borderline point-like sources, and  $-7, -9$  for problematic detections, e.g. sources partly saturated or whose magnitude is contaminated by bad-pixels inside the aperture used for the photometry extraction, or truncated because the source is very close to the mosaic borders. The astrometric accuracy in the source catalog is  $\sim 0''.2$  with respect to the UCAC4 catalog (Zacharias et al., 2013). Stellar sources typically show a FWHM of  $0''.6\text{--}0''.8$ . The instrumental magnitudes are obtained through aperture photometry and calibrated onto the VISTA system via non-saturated 2MASS stars in the field. Absolute photometric uncertainties are below 5% and the  $5\sigma$  limiting magnitudes, completeness and saturation limits in each filter are listed in Table 1 for the specific case of tile no. 12. The achieved magnitude limits in *JHK<sub>S</sub>*

<sup>2</sup> <http://apm49.ast.cam.ac.uk/surveys-projects/vista/vdfs>

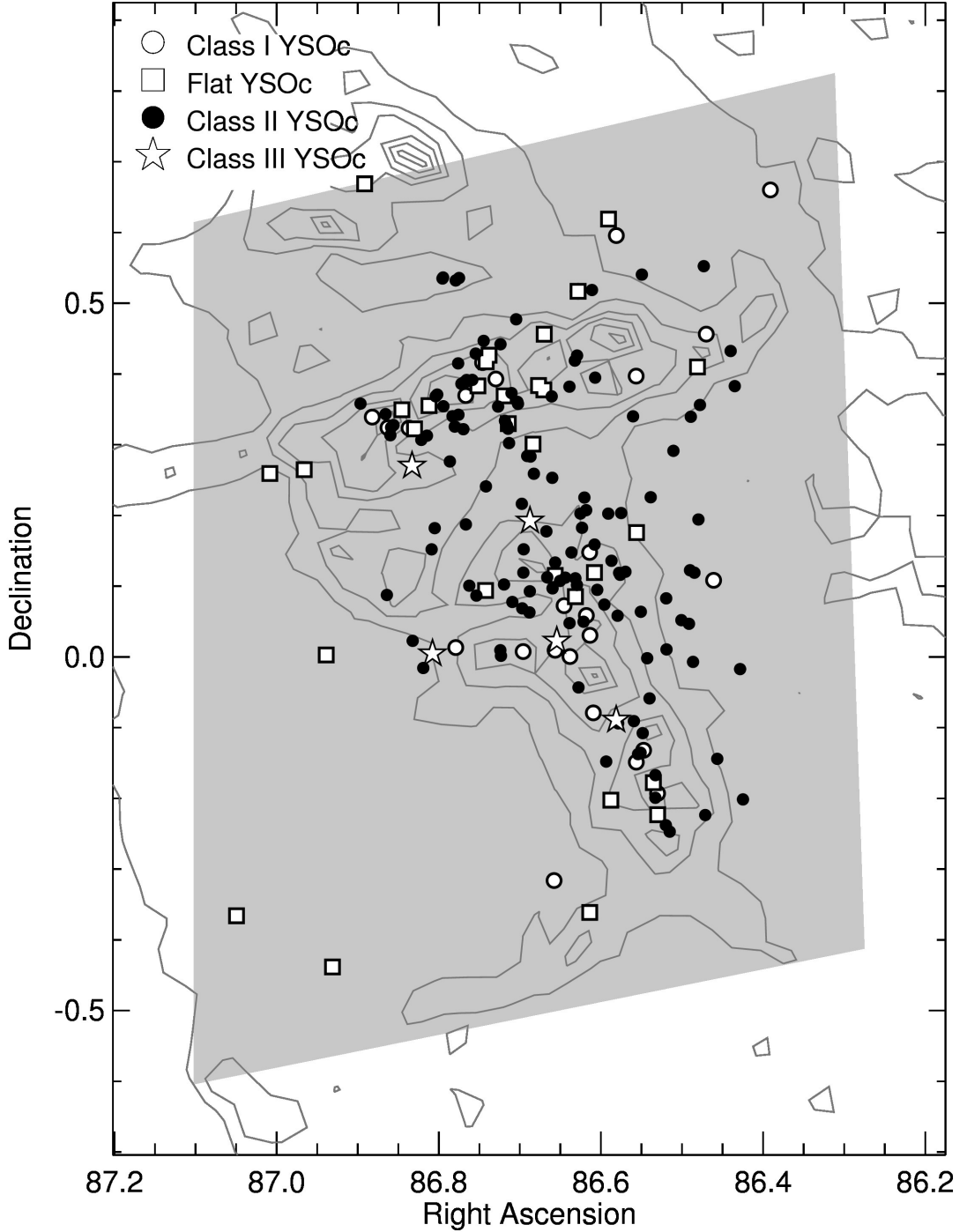


**Fig. 1.** Spatial distribution of the YSO candidates as a function of Lada classes over-plotted on the contours from the VISTA extinction map (solid lines). The contour levels of extinction ( $A_K$ ) are from 0.01 to 2 mag, in steps of 0.2 mag. The shaded area displays the regions observed with VISTA (tile no. 12).

are  $\sim 3$  mag deeper than 2MASS. The approximate completeness limit in each filter was derived as the point where the histogram of the magnitudes (Fig. 3) diverges from the dotted line, which represents the linear fit to the logarithmic number of objects per magnitude bin, calculated over the intervals of good photometric accuracy (Santiago et al., 1996; Wainscoat et al., 1992). In order to estimate stellar mass limits from our saturation and completeness limits, we compare with the theoretical isochrones by Baraffe et al. (1998) and Chabrier et al. (2000). Since the isochrones are provided for the Johnson-Cousins pho-

tometric system, which is different from the VISTA photometric system, we converted them to the VISTA photometric system as described in Appendix A. We estimate that our survey should have detected, for a population as young as  $\sim 2$  Myr at a distance of about 400 pc (i.e., the case of L1630 N) essentially all objects from  $\sim 1 M_\odot$  down to  $\sim 5$  Jupiter masses ( $\sim 0.0045 M_\odot$ ) in a region showing less than 1 mag of visual interstellar extinction.



**Fig. 2.** VISTA three colour (ZJKs) mosaic image of L1630 N on a logarithmic display. The image covers the grey shaded area of Figure 1.

## 2.2. *Spitzer* data

The Orion clouds were observed by the *Spitzer* Space Telescope (Fazio et al., 2004; Rieke et al., 2004) as part of the Guaranteed Time Observation (GTO) programs PID 43, 47, 50, 58, 30641, and 50070. The extraction of point source photometry from this survey in the four IRAC bands and the MIPS  $24\mu\text{m}$  band and an overview of the basic properties of the resulting point source catalog have been presented by Megeath et al. (2012). The catalog

contains 298405 sources that are detected in at least one of the IRAC bands or in the MIPS  $24\mu\text{m}$  band, the limiting magnitudes at the  $10\sigma$  level are roughly 16.5, 16.0, 14.0, 13.0 and 8.5 at 3.6, 4.5, 5.8, 8 and  $24\mu\text{m}$ , respectively (see Fig. 2 by Megeath et al., 2012). The catalog exhibits spatially varying completeness due to confusion with nebulosity and crowding of point sources in dense clusters (see Fig. 3-4 by Megeath et al., 2012). The Orion IRAC/MIPS maps are broken into several fields centered on the regions of strong  $^{13}\text{CO}$  emission (Miesch & Bally, 1994).



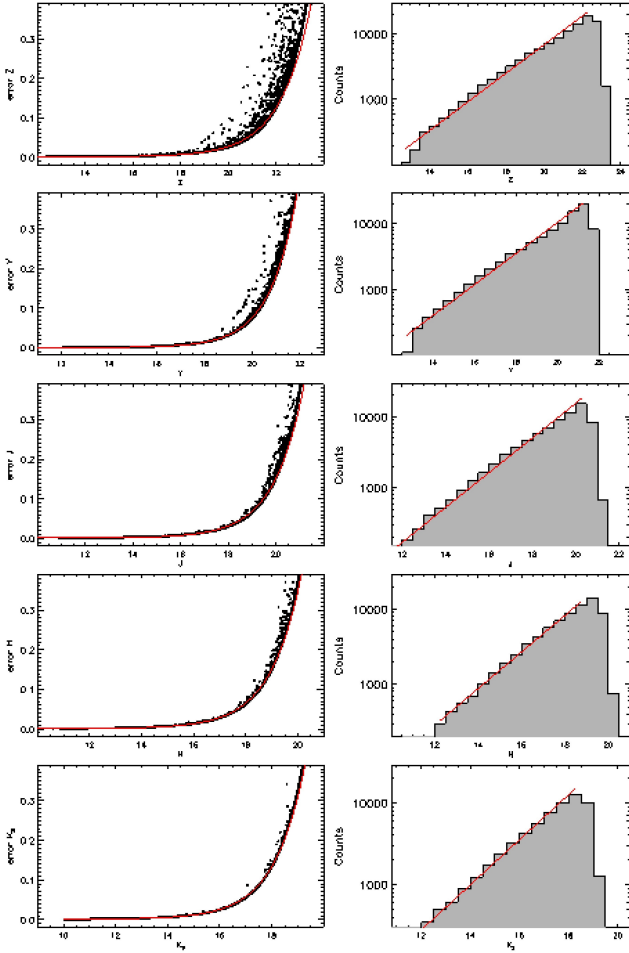


**Fig. 3. Left panels:** Photometric errors as a function of magnitudes and relative exponential fit (continuous line) for non-saturated sources detected by the VISTA Orion Survey tile no. 12 in the  $ZYJHK_S$  filters. **Right panels:** Number of detection as a function of magnitude. The line shows the linear fit to the logarithmic number distribution of magnitudes, which is used to find the turning point of the distribution, indicating our completeness limit.

We used a sub-set of the general catalog covering an area of  $2.58 \text{ deg}^2$  around L1630 N.

### 3. Selection of YSO candidates

The  $J - H$  vs.  $H - K_S$  color-color (CC) diagram is traditionally used to select low-mass YSO candidates (YSOc) on the basis of near-IR data, because young K/M type stars exhibit a narrow range of colors in this diagram and, in particular, an  $H - K_S$  excess mainly arising from their circumstellar disk and/or in-falling envelope (Meyer et al., 1997; Luhman & Rieke, 1999; Lee et al., 2005). However, near-IR colors of YSOs may be mimicked, to some extent, by highly reddened stellar photospheres of older main-sequence dwarf stars in the field and, hence, the selected sample might be contaminated. On the other hand, the identification of YSOs on the basis of mid to far-IR colors alone is not trivial, because the YSO colors in this wavelength regime are very similar to those of many background galaxies (Sect. 3.1 by Evans et al., 2009). Thus, to select YSOs in L1630 N we adopt the approach by Harvey et al. (2007a), based on the combined use of  $JHK_S$  photometry and *Spitzer* IRAC/MIPS colors.

By using *Spitzer* observations of the Serpens star forming region and the SWIRE catalog of extragalactic sources (Lonsdale et al., 2003), these authors defined the boundaries of the disk-bearing YSO locus in several IRAC/MIPS color-magnitude and CC diagrams. Their criteria have proven to provide an optimal separation between disk-bearing YSOs (mainly class II, class I and Flat Spectrum objects), reddened field stars and galaxies, with the fraction of remaining contaminants (mainly background field dMe dwarfs, a few K/M-type giants, and Be and AGB stars) estimated to be around 30% (e.g., Spezzi et al., 2008; Oliveira et al., 2009; Cieza et al., 2010). These criteria have been applied to select YSO candidates in all star forming regions observed within the frame of the *Spitzer* c2d (Evans et al., 2009) and *Spitzer* Gould Belt<sup>3</sup> Legacy surveys (e.g., Spezzi et al., 2011; Hatchell et al., 2012; Dunham et al., 2013).

We first matched our VISTA catalog for tile no. 12 with the *Spitzer* catalog by Megeath et al. (2012) using a matching radius of  $3''$ , larger than the astrometric accuracy of our mosaics (Sect. 2.1) and corresponding to twice the typical FWHM of sources in IRAC maps<sup>4</sup>. Then, we applied the YSO selection method by Harvey et al. (2007a) to the matched catalog, containing  $\sim 58500$  sources with complete  $ZYJHK_S$ , IRAC 3.6, 4.5, 5.8 and  $8 \mu\text{m}$  and MIPS-24  $\mu\text{m}$  photometry. A detailed review of the selection method can be found in Harvey et al. (2007a,b). Briefly, the selection method consists in the definition of an empirical probability function which depends on the relative position of a given source in several CC and CM diagrams, where diffuse boundaries have been determined to obtain an optimal separation between YSOs and galaxies. Figure 4 (left panels) shows the VISTA/*Spitzer* CC and CM diagrams used to select the YSO candidates in L1630 N. Note that the method requires detection in all IRAC bands and in MIPS-24  $\mu\text{m}$  with a S/N higher than 3 to classify an object as a YSO candidate or a background galaxy. Diskless YSOs, i.e. class III sources, are usually rejected by the selection method. Moreover, older field objects with no IR excess emission are rejected *a priori* because their IR colors are comparable with normal photospheric colors, e.g.,  $K_S - [4.5] < -0.1$ ,  $[8] - [24] < 0.1$ ,  $[4.5] - [8] < 0.2$  (Harvey et al., 2007b). In addition to the criteria by Harvey et al. (2007a), we used the VISTA morphological parameter (FLAG; Sect. 2.1) to distinguish between point-like (FLAG=-1) and extended (FLAG=1) YSO candidates; YSO candidates truncated and/or contaminated in VISTA pass-bands ( $-9 \leq \text{FLAG} \leq -2$ ) could not be classified. We note that, although clearly extended sources in the VISTA mosaic are more likely to be galaxies, we can not exclude them *a priori*, because YSOs still surrounded by significant circumstellar material might appear fuzzy/extended at IR wavelengths. Thus, we establish the YSO or galaxy nature on the basis of the above mentioned probability function alone, which depends exclusively on the VISTA/*Spitzer* colors of the sources.

We find 188 YSOc in L1630 N, shown in Figure 4 (left panels) as red dots, squares and asterisks for point-like, extended and morphologically unclassified sources, respectively.

#### 3.1. On the contamination of the YSOc sample

We adopted a statistical method to distinguish YSOs from extragalactic contaminants and field stars, hence, our candidates sample could be still slightly contaminated.

<sup>3</sup> <http://www.cfa.harvard.edu/gouldbelt>

<sup>4</sup> IRAC Instrument Handbook. See <http://irsa.ipac.caltech.edu/data/SPITZER/docs/irac/iracinstrumenthandbook/>

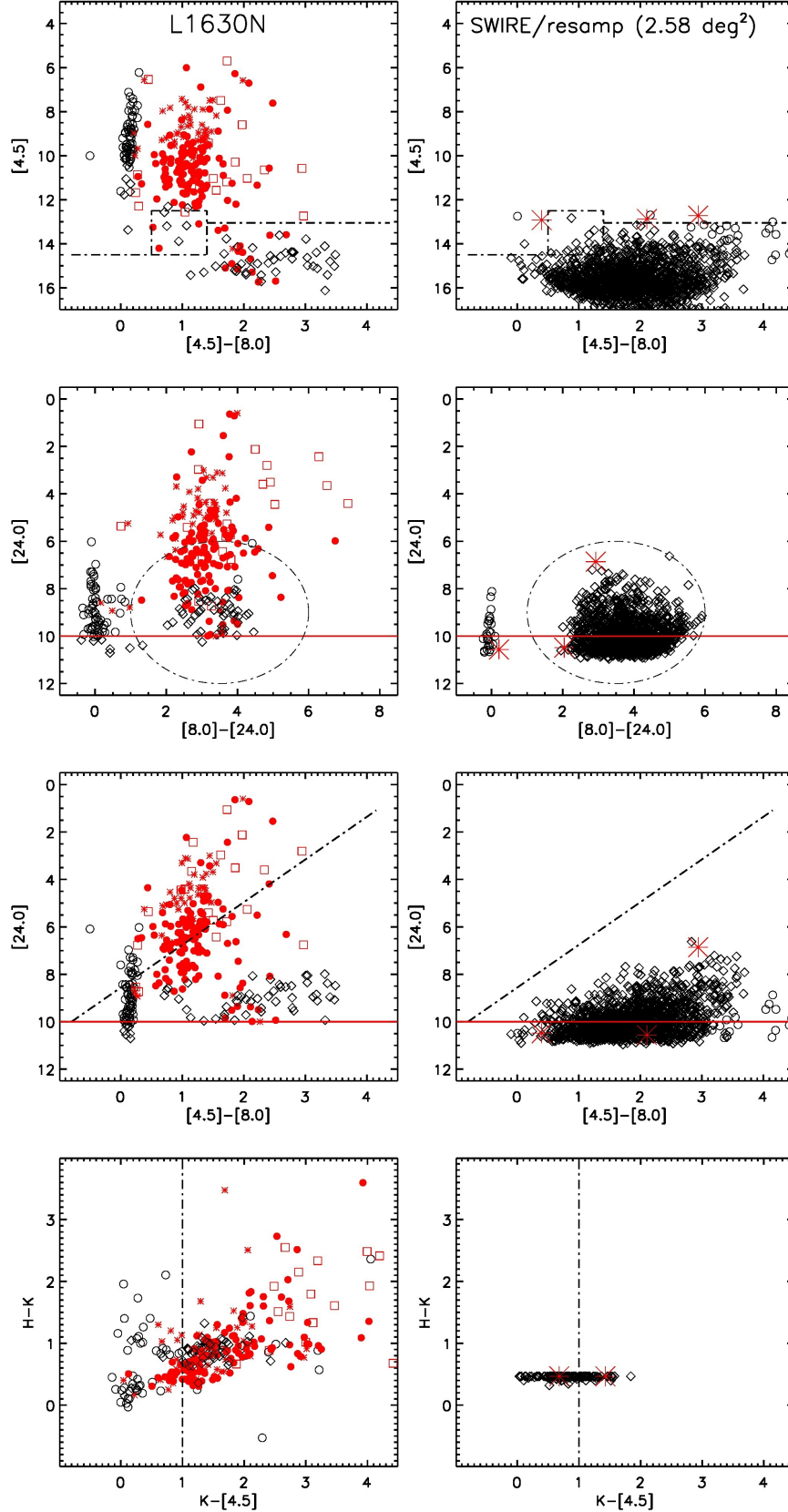


**Fig. 4.** **Left panels:** VISTA/*Spitzer* CM and CC diagrams for L1630 N. The dot-dashed lines show fuzzy limits with exponential cutoffs that define the YSO candidate selection criterion in the each diagram, excluding contamination from galaxy (diamonds) and field stars presenting normal photospheric colors (circles). The continuous lines show hard limits, objects fainter than which are excluded from the YSO category. Point-like and extended YSO candidates are indicated by dots and squares, respectively; YSO candidates with no VISTA morphological classification are indicated by asterisks. **Right panels:** 2MASS/*Spitzer* CM and CC diagrams for the SWIRE catalog (Sect. 3.1). Symbols are as in the left panels. Three objects of the SWIRE catalog (marked as asterisks) are classified as YSOc according to our selection criteria.

The number of interloping stars can be probed by using analytic models of the Galactic stellar distribution, i.e., simulations of the expected properties of stars seen towards a given direction of the Galaxy over a given solid angle. We performed this exercise by using the Galaxy model by Robin et al. (2003) and their online tool<sup>5</sup>. In the temperature range of our candidates, foreground stars are expected to be main-sequence cool dwarfs, whereas red giants are expected to dominate the background population. Assuming a cluster distance of 400 pc and a typical extinction of  $A_V \approx 1$  mag due to the L1630 N cloud itself, we expect some 50 foreground dwarfs in the  $1 \times 1.5$  square degree area observed in by VISTA (tile n. 12) with apparent  $K_S$  magnitude between 7 and 18.5 and spectral types of M0 to M9, i.e., the magnitude and spectral range corresponding to members of L1630 N detectable by our survey ( $\leq 1 M_\odot$ ; Sect. 2.1). Only a handful ( $\sim 3$ ) of background giants are expected to be found in the locus occupied by the cluster members because they generally appear much brighter than L1630 N members in the same effective temperature range. We thus conclude that only foreground cool main-sequence stars can contribute noticeably to the contamination of our candidate sample, but the contamination level is at most 25-30%. We note that contamination is higher ( $\sim 50\%$ ) in the substellar regime ( $\sim 0.1 M_\odot$ , i.e.,  $K_S \approx 13$  mag), and lower in the stellar regime ( $\sim 20\%$ ). On the other hand, as seen in Figure 1, the YSOs very clearly follow the cloud extinction contours which is not expected for a randomly distributed foreground population. Also, we find almost all of our YSOs consistent with infrared excess sources of class II or earlier (see Sect. 5). Therefore, we conclude that the true contamination of our sample is very low.

In order to have a statistical estimate of possible remaining extragalactic contaminants, we used the *Spitzer* Wide-area Infrared Extragalactic (SWIRE Surace et al., 2004) catalog coming from the observations of the ELAIS N1 field (Rowan-Robinson et al. 2004). The SWIRE catalog was trimmed and resampled as accurately as possible to match the spatial extent ( $2.58 \text{ deg}^2$ ) and sensitivity limits (Sect. 2.2) of the *Spitzer* observations in L1630 N. Moreover, the photometry of sources in the SWIRE catalog was edited in order to simulate the interstellar extinction in the direction of L1630 N, as expected on the basis of the VISTA extinction map (Sect. 7.1).  $JHK_S$  for the SWIRE sources are recovered from the 2MASS catalog (Skrutskie et al., 2006). For further details on how the trimmed resampled SWIRE comparison catalog was created, we refer the reader to Evans (2008) and Harvey et al. (2007a). The selection criteria applied to the comparison resampled SWIRE data lead to the conclusion that only 3 (i.e., less than 2%) of the selected YSO candidates in L1630 N may be background galaxies (Fig. 4). This result is similar to what Harvey et al. (2007a) and Alcalá et al. (2008) found for the Serpens and Cha II molecular clouds, respectively. Indeed, all the 188 candidates have been visually inspected in the VISTA images and we find that only two of them are clearly galaxies; these two candidates have been neglected in the subsequent analysis. All the remaining 186 candidates appear point-like or almost point-like in all our images and their photometry is not contaminated by nearby saturated stars, or any other artifact that might affect our selection criterion. A few of them ( $\sim 3\%$ ) present a close companion in the VISTA images not resolved in the *Spitzer* images and, hence, their *Spitzer* fluxes might be contaminated. We can not discharge *a priori* these candidates, because one or both objects in the system might still be young and, hence, responsible for the observed IR excess emission.

This leads us to a remaining caveat in our selection method. Our YSO candidates might be members of binary/multiple systems too close to be resolved with VISTA/*Spitzer* and, hence, affecting the measured photometry. As seen in Sect. 2.1, our candidates are expected to have masses  $\leq 1 M_\odot$ . The multiplicity fraction for stars in this mass regime is estimated to be between 20% and 40%, depending on the actual mass of the primary star and the separation range (Duquennoy & Mayor, 1991; Mason et al., 1998; Basri & Reiners, 2006; Lada, 2006). However, higher resolution imaging or spectroscopy would be needed to assess the actual multiplicity fraction in L1630 N.

### 3.2. Comparison with previous surveys

Before our study, a census of the young stellar population in L1630 N was presented by Flaherty & Muzerolle (2008) and by Fang et al. (2009). Flaherty & Muzerolle (2008) identified 69 cluster members with a rather spread spatial distribution, i.e., not confined to regions of dense gas and dust. For 67 of these members, they derived accurate spectral type and luminosity and estimated a median age of 2 Myr, and a large fraction of stars with infrared excess actively accreting (79%). Using a mix of criteria (presence of  $H\alpha$  emission, Li I absorption or IR excess) Fang et al. (2009) selected and analyzed 132 PMS stars in the general direction of the clusters. This list includes practically all the PMS stars studied by Flaherty & Muzerolle (2008). For 111 stars Fang et al. (2009) provide a classification in terms of their IR-excess as "thick disk, transitional disk, thin disk and no disk". Most of the 21 objects missing IR classification lack any information on Li I absorption and were selected as PMS stars by Fang et al. (2009) only because  $H\alpha$  is detected in emission, although rather weak considering their spectral types (White & Basri, 2003).

Our YSOc sample consists of 186 objects. In Table A.2 we report their coordinates and VISTA + *Spitzer* photometry. The VISTA/*Spitzer* selection criteria recovered 50 out of the 69 (i.e.  $\sim 75\%$ ) PMS stars listed by Flaherty & Muzerolle (2008), specifically 10 weak T Tauri stars (WTTs) and 40 classical T Tauri stars (CTTs). Likewise, our criteria recover 82 of the 132 objects in Fang et al. (2009) (i.e.,  $\sim 62\%$  of the whole sample, but 74% of the sample with IR classification). Most of the recovered objects by the VISTA/*Spitzer* selection criteria in both catalogs can be classified as Class II YSOs. Our survey missed about 50 of the previously known YSOs in the area, i.e.  $\sim 21\%$  of the YSO population (50 of  $186+50$ ), the vast majority of which are WTTs or objects without disks, i.e. Class III YSOs. We mark in Table A.2 the YSOs already identified by Flaherty & Muzerolle (2008) and/or Fang et al. (2009).

Although the selection criteria and color cuts presented here are different from those by Megeath et al. (2012) it is also interesting to compare our results with their selection, since we gathered the *Spitzer* photometry from their catalog (see Section 2.2). In our studied area there are 257 sources selected by Megeath et al. (2012) as possible YSOs, but 75 of these lack information in at least one IRAC band or at  $24 \mu\text{m}$ . Since our selection criteria require the detection in all IRAC bands and at  $24 \mu\text{m}$ , we can classify 182 of the Megeath et al. (2012) sources in the region. With our methods we thus recover 162 YSOs, meaning that our criteria miss 20 of the Megeath et al. (2012) sources. Most of them are classified as possible protostar candidates by Megeath et al. (2012) and are distributed in regions of high stellar density. Thus, our criteria recover about 90% of the Megeath et al. (2012) sources.

<sup>5</sup> <http://model.obs-besancon.fr/>

#### 4. Luminosity Function and Characteristic Stellar Mass

The stellar luminosity can be used as a poor but still useful first-order proxy for mass, assuming that most of the stars have formed more or less at the same time. Before using the range of luminosities to provide an estimate of the mass range, we determined the degree of completeness of the YSO candidate sample in L1630 N. Our selection criteria ultimately rely on the VISTA and *Spitzer* IRAC 3.6-8 $\mu$ m/MIPS 24 $\mu$ m detection of the objects and on the quality of this detection. Thus, in order to investigate the expected number of low-luminosity objects and infer the typical mass distribution of our YSOc sample, we have to take the completeness of these two datasets into account.

##### 4.1. 1-30 $\mu$ m Bolometric Luminosity Function

In order to estimate the completeness of the *Spitzer* observations in the L1630 N, we used the same approach as Harvey et al. (2007a), which has been applied to all c2d/GB clouds (e.g., Alcalá et al., 2008; Merín et al., 2008; Spezzi et al., 2011).

We derive first the total infrared luminosity of our YSOc by integration over their SED flux between 1 to 30  $\mu$ m; the total flux was converted to luminosity assuming a distance of 400 pc. We then applied the Harvey et al. (2007a) completeness correction factors for the c2d survey to our YSO candidate samples. Harvey et al. (2007a) estimated the completeness of the c2d catalogs by comparing, for each luminosity bin, the number of counts from a trimmed version of the deeper SWIRE catalog of extragalactic sources (assumed to represent 100% completeness by c2d standards) with the number of counts for the c2d catalogs in Serpens. This completeness correction can be applied to our *Spitzer* catalog of L1630 N because its photometric depth (Sect. 2.2) is similar to the one of the c2d catalogs (in both cases the  $10\sigma$  limit is  $\sim 16.5$  mag for IRAC 3.6 $\mu$ m and  $\sim 8.5$  mag for MIPS 24 $\mu$ m; compare Fig. 23 and 26 by Evans (2008) with Fig. 2 by Megeath et al. (2012)). Figure 5 shows the 1-30 $\mu$ m bolometric luminosity function (BLF) for YSOc in L1630 N before (solid line) and after (dashed line) correction for completeness, and suggests that we are missing only a few ( $<5$ ) of additional low-luminosity sources with  $\log(L/L_\odot) < -1.7$ . These objects have been missed by our selection either because they are below the noise level of the *Spitzer* observations or because they are located within the galaxy loci of the CM diagrams (Fig. 4). In conclusion, our YSO candidate samples in L1630 N is fairly complete. The luminosity histogram suggests a completeness better than  $\sim 95\%$  at luminosities down to  $0.01 L_\odot$ , which correspond to a mass of  $0.02 M_\odot$  for 2 Myr old stars according to the PMS evolutionary tracks by Baraffe et al. (1998) & Chabrier et al. (2000). The peak of the luminosity function appears at  $0.25 L_\odot$ , which corresponds to a  $0.4 M_\odot$  star (i.e., spectral type M3 at an age of 2 Myr). A very peculiar characteristics of the L1630 N 1-30 $\mu$ m bolometric luminosity function is that it shows a significant number ( $\sim 35\%$ ) of low- and very low-luminosity objects ( $\log(L/L_\odot) \lesssim -1$ ). A similar tail of low-luminosity objects was noted in the Lupus I, III and IV star forming regions ( $\sim 40\%$  Merín et al., 2008; Comerón, 2008), while it is not observed in other c2d/GB clouds such as Cha II ( $\sim 15\%$  Alcalá et al., 2008), Lupus V and VI (10-20% Spezzi et al., 2011) and Serpens (Harvey et al., 2007a).

##### 4.2. K-band Luminosity Function

To further investigate/confirm the stellar mass distribution of the L1630 N YSO population, we also constructed its K-band lumi-

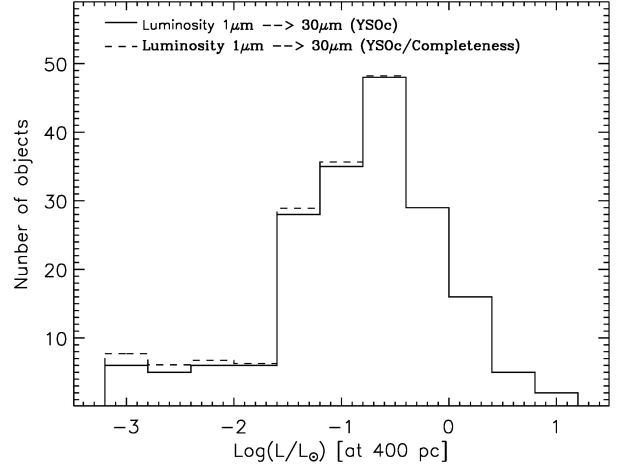


**Fig. 5.** Luminosity distribution for the YSOc in L1630 N (solid histogram). The plotted luminosities were determined as in Harvey et al. (2007a), i.e., by integration of the SEDs from 1 to 30  $\mu$ m. The corrected luminosity distribution, determined by applying completeness factors at each luminosity bin as in Harvey et al. (2007a), is over-plotted (dashed histogram).

nosity function (KLF). We choose the KLF rather than the *J* or *H*-band luminosity functions in order to minimize the effects of extinction, to maximize our sensitivity to intrinsically red, low-luminosity members of this cluster, and to make detailed comparisons to the KLF of the nearby Trapezium cluster presented by Muench et al. (2002). We did not correct the K-band fluxes for excess emission, but this should not affect the comparison with the Trapezium Cluster KLF, because Muench et al. (2002) do not correct for disk excess flux neither. The majority of stars in the Trapezium sample are disk-sources, and the H-K color distribution of the whole Trapezium sample is very similar to the H-K color distribution of our YSO sample in L1630, indicating a similar disk excess nature for the samples.

In Figure 6 we present the observed and dereddened KLF of L1630 N. We use relatively wide bins (0.5 mag) that are much larger than the photometric errors (Fig. 3) and adopt for each YSOc the visual extinction derived from the VISTA extinction map (Sect. 7.1) and reported in Table A.2. The K-band excess could add  $\sim 0.5$  mag, on average, to the observed K-band magnitude (Meyer et al., 1997), i.e. about the same size as the KLF binsize. However, this does not have any significant affect on our conclusions on the KLF shape, as the excess is a property over the entire luminosity range (i.e. there is no singular effect on an individual mass regime of the KLF), and the steady decline in the sub-stellar regime discussed below is a robust result. We also indicate in Figure 6 the *K*-band saturation limit and limiting magnitude of our VISTA catalog (Table 1) and overplot, for comparison purposes, the Trapezium KLF as derived by Muench et al. (2002), arbitrarily scaled to the peak of the L1630 N KLF.

The KLF of L1630 N shows a broad peak between 10.5 and 12 mag, i.e.,  $0.3$ - $0.7 M_\odot$  at the cluster distance and age according to the 2 Myr isochrone by Baraffe et al. (1998) & Chabrier et al. (2000) converted to the VISTA photometric system (Appendix A). Then, it steadily declines to the Hydrogen-burning limit ( $\sim 0.1 M_\odot$ , i.e.,  $K_S \approx 13$  mag). Below this limit,



we count a fraction of 28% substellar YSOs<sup>6</sup>. However, we note that the expected contamination from field stars mimicking the colors of BDs is expected to be  $\sim 50\%$  (Sect. 3.1), while it is lower in the stellar regime ( $\sim 20\%$ ) and, hence, the actual fraction of sub-stellar objects in L1630 N could be as low as 20%. Thus, the KLF of L1630 N indicate a stellar mass distribution consistent with the 1-30  $\mu\text{m}$  BLF. Moreover, it appears remarkably similar to the Trapezium KLF (see Fig. 11a by Muench et al., 2002), which presents a broad peak around  $0.6 M_{\odot}$  and then declines into the sub-stellar regime, the fraction of sub-stellar objects being  $\sim 22\%$ . Muench et al. (2002) also reported a significant secondary peak around 10-20 Jupiter masses ( $\sim 0.02 M_{\odot}$ ). Although we do observe a similar fraction of sub-stellar objects, the presence of this secondary peak is not obvious in the KLF of L1630 N, which appears to keep its steady decline down to our completeness limit ( $\sim 0.0045 M_{\odot}$ , i.e.,  $K_S \approx 18.5$  mag).

The mass function shape of the Trapezium cluster in the sub-stellar regime has been long debated, because the large fraction of brown dwarfs (BDs) with respect to other nearby star forming regions ( $\sim 15\%$ ; Briceño et al., 2002; López Martí et al., 2004; Spezzi et al., 2007, 2008, 2009) could be an affect of spatial and photometric incompleteness of the surveys conducted so far. However, more and more complete surveys are now available and, still, there is no universal agreement on the behavior of the mass function over the substellar regime. For a complete collection of BD fraction measurements in nearby star forming regions and a discussion on possible trends, we defer the reader to Scholz et al. (2012) and references therein. Note that these authors compare the star-to-BD ratio ( $R_{\text{star}/\text{BD}}$ ) for various star-forming region (see their table 5). It appears more and more evident that, on one hand, there are clusters like IC 348, T association like Taurus, Chamaeleon,  $\rho$ -Ophiuchus, etc., with a low number of sub-stellar objects ( $R_{\text{star}/\text{BD}}$  in the range 5 to 8), and on the other hand there are more massive clusters such as Trapezium, the Orion Nebula Cluster (ONC), NGC 1333, Upper Scorpius, etc., where this number is much higher ( $R_{\text{star}/\text{BD}} \approx 2-4$ ). L1630 N, as other clusters in the Orion complex (Trapezium and the ONC), would belong to this last category, with  $R_{\text{star}/\text{BD}} \approx 2.5-3.9$  depending on the actual contamination level. The variation of the fraction of substellar objects observed from region to region possibly indicates environmental effects on their formation mechanism, a key point of the current star formation theory still under debate (e.g., Whitworth et al., 2007).

## 5. Lada classes, disk fraction and disk lifetimes

In this section we revise the disk properties of the young stellar population in NGC2068/2071 on the basis of our YSO candidates sample, and in comparison with the results by Flaherty & Muzerolle (2008).

In order to investigate the disk properties of our YSO candidate sample, we adopted the Lada classification (Lada & Wilking, 1984) based on the SED slope ( $\alpha$ ) of the line joining the flux measurements at  $2.2 \mu\text{m}$  (K-band) and MIPS-24  $\mu\text{m}$ . In particular, we used the Lada's class separation as extended by Greene et al. (1994), i.e.  $\alpha \geq 0.3$  for Class I,  $-0.3 \leq \alpha < 0.3$  for flat-spectrum sources,  $-1.6 \leq \alpha < -0.3$  for Class II sources, and  $\alpha < -1.6$  for Class III sources. We report in Table A.2 the Lada class computed for each YSOc and give in Table 2 the statistics for the entire YSOc sample in L1630 N. As shown in Figure 7, the dominant objects in L1630 N are those of Class

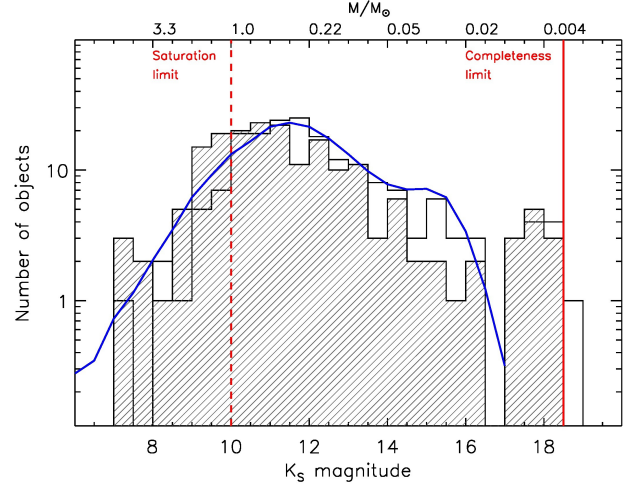


**Fig. 6.** The L1630 N K-band luminosity function (KLF) before (empty histogram) and after correction for interstellar extinction (line-filled histogram). The labels in the top x-axis indicate the corresponding stellar mass according to the VISTA 2 Myr isochrone (Appendix A). The continuous and dashed vertical lines indicate the completeness and the saturation limit of the VISTA K-band photometry, respectively. The continuous curve is the KLF of the Trapezium cluster (Muench et al., 2002), scaled to the peak of the L1630 N KLF.

**Table 2.** Summary of Lada Classes in L1630 N and estimated lifetime for each phase.

Lada class	n. of YSO candidates	lifetime (Myr)
I	25 (13%)	0.40
Flat	30 (16%)	0.48
II	126 (68%)	2 <sup>†</sup>
III	5 (3%)	–

<sup>†</sup> Assumed lifetime for the Class II phase (Evans et al., 2009).

II (68%), followed by flat-spectrum (16%) and Class I (13%) sources, with only a minority being Class III sources (3%). The distribution of YSOs over class supports the young age estimated for this star-forming region. The ratio of the number of Class I and flat-spectrum sources to the number of Class II and Class III sources is 0.42, similar to the ratio measured in Serpens (Harvey et al., 2007a) and other clouds of similar age surveyed by the *Spitzer* c2d survey (Evans et al., 2009). The total observed fraction of objects with thick disks and/or envelope (Class I to II) for our sample is on the order of 97%, while those with thin or no disk (Class III) represents only  $\sim 3\%$  of the sample. The total disk fraction is considerably higher than the values derived in other regions of similar age (e.g., in IC 348; Lada, 2006) and this would make L1630 N a clear outlier with respect to the typical disk fraction vs. age trend (e.g., see Fig. 1 and Fig. 4 by Haisch et al., 2001; Fedele et al., 2010, respectively).

Contamination from field stars, which could be as high as 25-30% (Sect. 3.1) should not heavily affect the relative number of object with and without disk, because there is no reason to assume that this kind of contamination affects one Lada class more than the others. Background galaxies preferentially mimic the colors of YSOs with thick disks/envelope, but they may account for 2% of our YSOc sample at most and can not justify the high number of Class I to II objects.

<sup>6</sup> This fraction is computed as the number of substellar objects over the total number of YSOc.

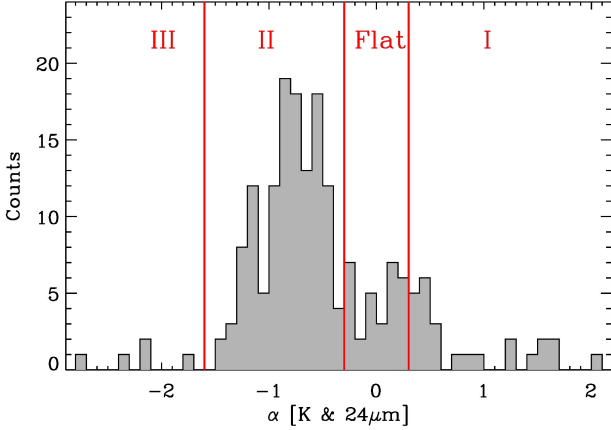


**Fig. 7.**  $\alpha$ -slope distribution of YSOs in L1630 N. The vertical lines indicate the intervals defining the four Lada classes. The population is largely dominated by Class II objects.

However, one may wonder whether our census might have missed a significant number of diskless YSOs. This would be possible because the c2d criteria select only IR excess objects. A direct way to investigate the number of diskless YSOs missed in our survey is to compare our results with those of deep X-ray observations, which are the most secure way to trace the population of class III objects. By the merging of many *Chandra* pointed observations in a region centered between NGC 2068 and HH24-26, Principe et al. (2014) obtained a very deep X-ray image with an equivalent exposure time of about  $240 \times 10^3$  sec. In an area of about 0.12 square degrees they detected 52 X-ray sources, 32 of which can be identified with class III or transition objects. Six of these objects have been recovered in the same area by our selection, but five were classified as Class III and one as Class II by our work. Considering that transition objects may mimic colors of Class III objects, the conclusion is that our selection misses a factor of about 5 or 6 the actual number of diskless YSOs. This is in perfect agreement with the estimated number of missed diskless YSOs in the c2d surveys (see Sect. 3.2 in Evans et al., 2009). Hence, we are most likely missing 25-30 class III YSOs (i.e.  $\sim 20\%$ ) in our sample (see Table 2), which is also consistent with the fraction of diskless YSOs missed by our criteria in the Flaherty & Muzerolle (2008) and Fang et al. (2009) samples (see Sect. 3.2). Certainly, in order to obtain a real full census of class III objects in the area a much larger scale deep X-ray survey would be needed. But since such observations are currently not available we use the above correction as a first order estimate, which leads to an expected fraction of class III YSOs in L1630 N predicted by our data of  $\sim 15\%$ . This is still lower than expected on the basis of a cluster age of 1-2 Myrs.

The surveys for PMS objects by Flaherty & Muzerolle (2008) and Fang et al. (2009) produced a similar result on the high fraction of YSOs with disks and envelopes. Their surveys are rather complete in both space and flux and are based on different selection criteria, i.e., location on optical/near-IR color-magnitude diagram with respect to the expected position of the main sequence at the cluster distance and subsequent spectroscopic follow-up. Flaherty & Muzerolle (2008) report a fraction of strong disk (Class I/II) of 66% and a fraction of MIPS-weak disks of 16%, in perfect agreement with our fraction of disk objects after applying the correction of missed class III sources.

They also find a fraction of IRAC-weak disks (Class III) of  $20 \pm 8\%$ , higher than our estimate but still lower than the fraction of Class III YSOs found in regions of similar age. Similarly, Fang et al. (2009) report a high fraction ( $\sim 80\%$ ) of disks in the region, although this value might also be biased by their selection which preferentially selects disk bearing young stars.

Alternatively, the substantial number of objects in younger SED classes is due to still ongoing star formation in L1630 N, and correspondingly young age ( $\leq 1$  Myr) for the studied YSO samples. As we will see in Sect. 7.3, some studies (Lada et al., 2010; Heiderman et al., 2010) have revealed that, if most of the present-day mass measured for a given cloud lies below a certain gas surface density threshold, which was determined by Heiderman et al. (2010) to  $\sim 129 M_{\odot} \text{pc}^2$  (corresponding to  $A_V \approx 8.6$  mag), a decrease in star formation could plausibly be caused by exhaustion of gas above such a threshold in surface density. Spezzi et al. (2011) demonstrated that this is the case for some clouds in the Lupus complex (Lup V and VI), where only  $\sim 1\%$  of the cloud mass lies above the threshold and, consistently, older SED classes (Class III) dominate the YSO population, while other Lupus clouds with 5 to 25% of the cloud mass above the threshold are mainly populated by younger SED classes (Class I to II). The fraction of cloud mass above the threshold in L1630 N is  $\sim 35\%$  (Table 4), i.e., even higher than in the most active star-forming region of Lupus (Lupus III), and may explain its exceptionally high disk fraction.

Thus, although the actual value might be slightly lower, the result on the high disk fraction in L1630 N seems to be real. The average disk fraction vs. age trend reported in the literature (e.g., Fedele et al., 2010) suggests a median disk lifetime around 2-3 Myr, meaning that  $\sim 50\%$  of the stars in a given population should have lost signatures of their disks after this time. However, several cases of clear outliers with respect to the average disk fraction vs. age trend have been reported in the literature. For example, Alcalá et al. (2008) found that only about 20%-30% of YSOs in Chamaeleon II have lost their primordial disks in about 4 Myr (i.e., the average age for its members), and Sicilia-Aguilar et al. (2006, 2013) measured a disk fraction of  $\geq 50\%$  in the coeval cluster Trumpler 37. Moreover, studies in NGC 3603 (Beccari et al., 2010) and the Magellanic Clouds (Spezzi et al., 2012; De Marchi et al., 2011a,b) indicate that a considerable fraction of PMS stars still exhibit signatures of accretion from a circumstellar disk at ages as old as 10 Myr. It is still under debate whether these differences from region to region are due to residual incompleteness effects of different surveys, limitations of the adopted selection methods, etc., or to the specific properties of the given star-forming environment (such as metallicity, presence of strong UV radiation fields, multiplicity, crowding, etc.), which may strongly affect disk evolution (e.g., Hollenbach et al., 2000; Linsky et al., 2007; Dullemond & Dominik, 2005; Johansen et al., 2009; Daemgen et al., 2013).

Evans et al. (2009) derived the half-life for each of the Lada classes from the combined analysis of the Spitzer c2d data set. According to this study, the half-life for Class II sources is  $\sim 2$  Myr. If star formation has been continuous over a period longer than the age of Class II sources, the lifetime for each phase can be estimated by taking the ratio of number counts in each class with respect to Class II counts and multiplying by the lifetime for Class II. According to the statistics of Lada classes in L1630 N, we estimate a lifetime of 0.4 and 0.48 Myr for the Class I and Flat-spectrum phase, respectively (Table 2). These values agree with the lifetimes derived by Evans et al. (2009) by averaging all c2d clouds.

**Table 3.** Results of the clustering analysis and properties of star formation in sub-structures in Lynds 1630 N

Region	#YSOs	# IR Class				Mass ( $M_{\odot}$ )	$\langle A_V \rangle$ (mag.)	SFE %	Area ( $\text{pc}^2$ )	Mass/Area ( $\Sigma_{\text{gas}}$ ) ( $M_{\odot} \text{pc}^{-2}$ )	SFR/Area ( $\Sigma_{\text{SFR}}$ ) ( $M_{\odot} \text{Myr}^{-1} \text{pc}^{-2}$ )
		I	Flat	II	III						
Extended	15	4	3	6	2	1840	0.3	0.4	...	...	...
Lynds 1630 N	171	21	27	120	3	2050	4.8	4.0	20.2	102	2.0
...NGC 2071	52	5	12	34	1	400	8.8	3.8	2.17	180	6.0
...NGC 2068	45	4	5	36	0	243	5.5	5.3	2.12	115	5.4
...HH24-26	14	6	2	5	1	124	7.7	3.3	0.77	161	4.6

## 6. Spatial Distribution and Clustering

The spatial distribution of the different classes of objects in L1630 N is shown in Figure 1 over-plotted on the VISTA extinction map, derived as explained in Sect. 7.1. The Class I and Flat sources coincide or are located close to the sites of highest extinction, as observed in all young clusters still associated with the residual parental clouds.

NGC 2068 and NGC 2071 are the most prominent star-forming clusters in the L1630 N molecular cloud. The VISTA extinction map shows, in a consistent way, two extinction peaks corresponding to the approximate center of NGC 2068 (R.A.  $\approx 86.65$  deg, Dec.  $\approx 0.1$  deg) and NGC 2071 (R.A.  $\approx 86.75$  deg, Dec.  $\approx 0.35$  deg). It is also evident that, beside these two peaks, there is an additional extinction peak centered at R.A.  $\approx 86.55$  deg and Dec.  $\approx -0.15$  deg. This third peak corresponds to the HH 24-26 group of Herbig-Haro objects, and is very close to V1647 Ori (see Fig. 7 by Gibb, 2008), a low-luminosity protostar, perhaps in a transition phase from Class I to Class II which underwent a strong outburst in 2004 (Briceño et al., 2004). We also observe a very clear concentration of Class I and Flat sources around this peak, confirming that the region is one of the several small centers of star formation in L1630. Another argument for still actively ongoing star formation, is a notable concentration of presumably very young protostars in the region (see Stutz et al., 2013).

Lada & Lada (2003) suggested that a cluster should be a group of some 35 members with a total mass density larger than  $1 M_{\odot} \text{pc}^{-3}$ . To compare with this criterion and in order to assess the sub-clustering structures in L 1630, it is important to examine the distribution of YSOs in a quantitative and uniform way. We calculated the volume density of YSOs, based on their Lada classes and position, using a nearest neighbor algorithm similar to the one applied by Gutermuth et al. (2005) and implemented by Jørgensen et al. (2008) for the c2d clouds. The calculations assume that the distribution of sources is locally spherical. We applied the algorithm to the whole sample of 186 YSOs in Table A.2. The overall results, reported in Table 3, are shown in Figure 8.

To define a cluster the c2d surveys adopted the tighter level of 25 times the Lada & Lada (2003) criterion (i.e., a mass density of  $25 M_{\odot} \text{pc}^{-3}$ ), which normally provides the already established cluster and group boundaries. Within the c2d surveys, "clusters" are regions with more than 35 YSOs within a given volume density contour and "groups" are regions with less. The lowest number of YSOs that is considered to constitute a separate entity is 5. "Clusters" and "groups" can be either "tight" or "loose" depending on whether their volume densities,  $\rho$ , are higher than 25 or  $1 M_{\odot} \text{pc}^{-3}$  (corresponding to 50 and 2 YSOs  $\text{pc}^{-3}$ ), respectively, assuming an average YSO mass of  $0.5 M_{\odot}$ . As noted in the c2d papers, these criteria are useful as a way of making direct comparison between regions within clouds and across different clouds, but being empirical they should not be used as

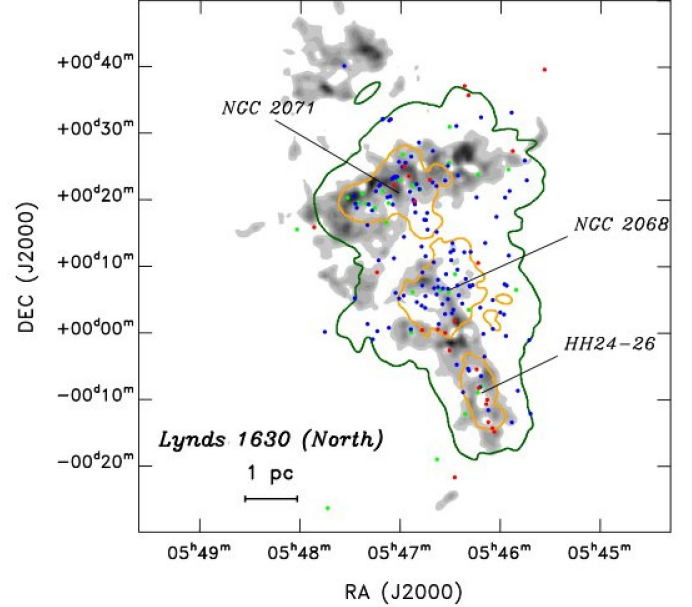


**Fig. 8.** Distribution of young stellar objects plotted over the extinction map (in gray) of the region. The green and orange contours correspond to volume densities of  $1 M_{\odot} \text{pc}^{-3}$  and  $10 M_{\odot} \text{pc}^{-3}$ , respectively. Class I sources are shown in red, Flat spectrum sources in green and Class II sources in blue.

evidence for discussions on whether the star formation process is hierarchical or not.

In L1630 N we identify structures with two levels of volume densities, structures with a density larger than  $1 M_{\odot} \text{pc}^{-3}$  (similar to the criterion for a cluster by Lada & Lada, 2003) or structures with a density as high as  $10 M_{\odot} \text{pc}^{-3}$ . Note, however, the latter is lower than what was applied for "tight" associations in the c2d surveys. Thus, according to the c2d criteria, the loose clusters identified in this region are L1630 N as a whole with a density of  $1 M_{\odot} \text{pc}^{-3}$  and NGC 2071 and NGC 2068 with a density of  $10 M_{\odot} \text{pc}^{-3}$ . The HH24-26 entity can be defined as a loose group with a density of  $10 M_{\odot} \text{pc}^{-3}$ .

## 7. Overall results on star formation in L1630 N

In this section we analyze and discuss the cloud properties of L1630 N and the global properties of star formation in this region on the basis of the VISTA observations and our YSOc sample. Our results are summarized in Table 4.

### 7.1. Extinction map, cloud mass and surface density

An extinction map, with a resolution of  $30''$ , was constructed for the entire area of Orion observed in the VISTA SV mini-



survey (Lombardi et al., *in prep.*). The technique used is optimized to produce highly accurate extinction maps from multi-band near-IR photometric data as outlined in Lombardi & Alves (2001, NICER) and Lombardi (2009, NICEST). The method is the natural generalization of the near-infrared color excess (NICE) method of Lada et al. (1994) and produces significantly less noisy and, hence, more accurate extinction maps taking advantage of all bands available. Applications of this technique to 2MASS data has shown an improvement with respect to the standard NICE algorithm of a factor 2 on the noise variance (Lombardi & Alves, 2001). We further compared our extinction map values with the spectroscopic values inferred by Flaherty & Muzerolle (2008) for a sample of 67 previously known PMS stars in the cloud and found a good agreement (within 2-3 visual mag), but also an apparent shift of  $A_V = 3.4$  mag (i.e. the extinction map gave a consistently higher  $A_V$  than what was determined from spectroscopy). This has been observed for other regions as well and can be explained by the fact that the extinction map measures the extinction through the *whole* cloud, while the PMS stars are located *in* the cloud.

According to this extinction map, the extinction in the L1630 N cloud (tile no.12) is typically low ( $A_V \approx 1$  mag), with peaks up to  $A_V \approx 20$  mag occurring close to the following locations: R.A.=86.75 deg & Dec.=0.35 deg (i.e., the center of NGC 2071), R.A.=86.65 deg & Dec.=0.1 deg (i.e., the center of NGC 2068) and R.A.=86.55 deg & Dec.=−0.15, where a group of YSOc has been identified by us (Sect. 6).

Using the extinction map and assuming a distance of 400 pc, we also estimated the cloud mass for the L1630 N complex. To this aim we used the relationship between gas surface density,  $\Sigma_{gas}$ , and extinction by Heiderman et al. (2010), i.e.  $\Sigma_{gas} = 15 \times A_V M_\odot/\text{pc}^2$ . We estimated that the total cloud mass for  $A_V \geq 2$  mag is about  $3865 M_\odot$ <sup>7</sup>; considering that the area where  $A_V \geq 2$  mag extends over  $\sim 39 \text{ pc}^2$ , the cloud column density is about  $\sim 100 M_\odot \text{ pc}^{-2}$ . The NICE and NICER methods provide an intrinsic error of about 0.5 mag, on the average. Assuming this value as the intrinsic error of our VISTA extinction map, and an error on the distance to the cloud of about 10% (see Sect. 2 in Gibb, 2008), we estimated that the cloud mass and column density of L1630 N can be safely placed in the ranges 3200–4600  $M_\odot$  and 81–116  $M_\odot \text{ pc}^{-2}$ , respectively.

We stress that in  $\sim 35\%$  of the cloud area where  $A_V \geq 2$  mag the extinction is above 8.6 mag. As concluded in Heiderman et al. (2010) the latter value for the extinction sets an important threshold at which the gas surface density is linearly proportional to the surface density of the star formation rate.

## 7.2. Star formation efficiency

We derive the global star formation efficiency (SFE) in L1630 N as:

$$SFE = \frac{M_{stars}}{M_{cloud} + M_{stars}} \quad (1)$$

where  $M_{cloud}$  is the cloud mass derived in Sect. 7.1, and  $M_{star}$  is the total mass converted into stars.  $M_{star}$  is derived from the number of YSOc identified in our study, i.e. without applying any corrections for missed diskless star, following the procedure applied by the *Spitzer*-c2d/GB surveys. As already pointed out by Evans et al. (2009), this implicates that the star formation efficiencies and rates over the whole star forming cloud's

<sup>7</sup> Note that the total mass of gas in dense cores in L1630 N has been estimated to be  $\sim 2000 M_\odot$  (see Sect. 3.1 in Gibb, 2008).

**Table 4.** Overall properties of the star formation in L1630 N .

Property	Value	Uncertainty Range	Unit
peak of the KLM	0.5	0.3-0.7	$M_\odot$
cloud area ( $A_V \geq 2$ mag)	39	–	$\text{pc}^2$
cloud mass ( $A_V \geq 2$ mag)	3865	3200-4600	$M_\odot$
cloud density ( $\Sigma_{gas}$ )	98	81-116	$M_\odot \text{ pc}^{-2}$
Fraction of cloud above $\Sigma_{th}$	0.35	–	
N. YSOc/Area	5	–	$\text{pc}^{-2}$
SFE	2.35	2-2.8	percent
SFR	75	47-103	$M_\odot/\text{Myr}$
SFR/Area ( $\Sigma_{SFR}$ )	1.9	1.2-2.6	$M_\odot \text{ Myr}^{-1} \text{ pc}^{-2}$

lifetime could be higher. For L1630 N we estimated  $M_{star}$  to be  $\sim 93 M_\odot$ , assuming an average YSO mass of  $0.5 M_\odot$  consistent with the peak observed in the KLF (Fig. 6), and with the assumption made in all clouds observed by the *Spitzer*-c2d/GB surveys, which we use for comparison.

We find that the overall SFE in L1630 N ranges between 2% and 2.8% and is  $\sim 4.0\%$  on average for the L1630 N clusters (Tab. 3), which is overall consistent with the typical values measured for Orion A and B (Federrath & Klessen, 2013, and references therein), for all c2d clouds (see Table 4 by Evans et al., 2009) and, more in general, for the majority of star-forming regions in the Galaxy (e.g., Federrath & Klessen, 2013). However, we notice that the SFE in L1630 N is lower than measured in the Orion bright-rimmed clouds (e.g., 5 to 10%; Lee et al., 2005) and, in particular, lower than measured in sub-clusters in the southern region L1630 S. For the populous cluster NGC 2024, Lada et al. (1997) determined a high SFE of  $\sim 30\%$ , although based on CS observations that trace only the highest density gas, and hence providing a lower cloud mass than the mass obtained by us via the extinction map method. It appears that the CS measurements underestimate the total cloud mass by a factor of 3-4 as compared to the cloud mass derived from the extinction map, such that the true SFE for NGC 2024 is likely more like  $\sim 10\%$ . In comparison, the SFE for the sub-clusters identified in L1630 N is very low (see Table 3). We recall that it is expected that star formation may be more efficient in localized, compressed regions, where triggered star formation might play a role, but perhaps not so in the entire cloud (Lee et al., 2005). The different SFE measured between the northern and the southern regions of L1630 might indicate that two different star-formation mechanisms currently dominate in the two regions of this cloud.

## 7.3. Star formation rate and star formation density

We derive the star formation rate (SFR) in L1630 N as:

$$SFR = \frac{M_{stars}}{Age} \quad (2)$$

where  $M_{star}$  is the total mass converted into stars (equal to  $\sim 93 M_\odot$ , Sect. 7.2) and  $Age$  is the average age of the YSO population. The latter has some uncertainty and therefore determines the possible range for the resulting SFR. A median age of 2 Myr was determined by Flaherty & Muzerolle (2008) for their optical spectroscopy sample in NGC 2068/71. However, this could be an overestimate for the L1630 N YSO sample in our work, which does include the large majority of the FM08 objects but also include highly embedded, i.e. potentially much younger, sources. Note that Fang et al. (2009) estimate a median age of 0.9 Myr for their YSO sample of L1630 N, of which 60% are included in our survey.

Taking the age uncertainty into account, we find that the L1630 N cloud is turning some  $75 \pm 28 M_{\odot}$  into YSOs every Myr. This SFR is in agreement with the SFR measured for the c2d/GB clouds (see Table 3 by Evans et al., 2009), with the exception of Cha II, where the SFR seems to be very low (Alcalá et al., 2008). However, the SFR in L1630 N appears lower than the average SFR measured for the overall Orion A and B molecular clouds ( $150\text{--}700 M_{\odot}/\text{Myr}$ ; see Table 2 by Lada et al., 2010) and the local SFR measured for the ONC (Lada et al., 1996) and Trapezium (Palla & Stahler, 1999; Lada & Lada, 2003). We note, however, that large SFR variations are observed among the Orion sub-regions; for example, the SFR in L1630 (to which L1630 N belongs) is known to be a factor of 2 to 7 lower than observed in the nearby L1641 (Meyer et al., 2008).

These variations can be reconciled if instead we consider the SFR per unit area ( $\Sigma_{SFR}$ ), i.e., the density of star formation. It has been confirmed that  $\Sigma_{SFR}$  is linearly proportional to the cloud gas surface density ( $\Sigma_{gas}$ ), above an extinction threshold of  $A_V \approx 8.6$  mag (Heiderman et al., 2010), corresponding to a gas density threshold ( $\Sigma_{th}$ ) of  $\sim 129 M_{\odot} \text{pc}^{-2}$ . We measure for L1630 N a  $\Sigma_{SFR}$  of  $1.9 M_{\odot} \text{Myr}^{-1} \text{pc}^{-2}$  and  $\Sigma_{gas}$  of  $\sim 98 M_{\odot} \text{pc}^{-2}$ , and these values are in excellent agreement with previous observations of galactic star-forming activity (Heiderman et al., 2010). Note also that, as mentioned in the previous section, about 35% of the cloud has  $A_V > 8.6$  mag. Thus, more than one-third of the cloud has a  $\Sigma_{gas}$  above  $\Sigma_{th}$ . At the level of the sub-structures identified in the clustering analysis, the values of  $\Sigma_{SFR}$  and  $\Sigma_{gas}$  are slightly higher (see Table 3) but still well within the range for galactic star-forming regions (Heiderman et al., 2010).

The linear correlation between the rate of star formation and the amount of dense gas in molecular clouds, confirmed by all c2d/GB clouds (Heiderman et al., 2010), all nearby molecular clouds (Lada et al., 2010), galactic massive dense clumps (Wu et al., 2010), the youngest and still embedded Class I and Flat-spectrum YSOs in the Galaxy (Heiderman et al., 2010), and also consistent with the results for several nearby molecular clouds (Gutermuth et al., 2011), lies above the extragalactic SFR-gas relations (e.g., Kennicutt-Schmidt law; Kennicutt, 1998) up to a factor of 17 to 54 (Heiderman et al., 2010). Moreover, the extragalactic SFR-gas relation is not linear, because  $\Sigma_{SFR}$  scales as  $\Sigma_{gas}^{1.4}$ . Several contributing factors to this difference have been identified so far (Heiderman et al., 2010): i) much of  $\Sigma_{gas}$  is below  $\Sigma_{th}$  in extragalactic studies, which average over large scales and include both star-forming gas and gas that is not dense enough to form stars, ii) using  $^{12}\text{CO}$  or  $^{13}\text{CO}$  to measure the  $\text{H}_2$  in galaxies gives systematically lower  $\Sigma_{gas}$  than Galactic  $A_V$  measurements, as the one we used, by a factor up to 30%. Indeed, power-law indices between 0.8 and 1.6 have been found for the extragalactic SFR-gas relation (e.g., Kennicutt et al., 2007; Bigiel et al., 2008; Krumholz et al., 2009), depending on the survey spatial resolution and the adopted tracer. These overall results suggest that the key to obtaining a predictive understanding of the star formation rates in molecular clouds and galaxies is to understand those physical factors which give rise to the dense components of these clouds (Lada et al., 2010).

## 8. Summary and conclusions

Based on the VISTA Orion mini-survey, complemented with Spitzer observations, we have performed a study of the YSO population and star formation in the L1630 N cloud. The c2d multi-color criteria selected 186 YSOs in the area of about 1.5 square degree in L1630 N. The census is  $\sim 95\%$  complete down to  $M_{\star} \sim 0.02 M_{\odot}$ . We have investigated both the YSOs

with infrared excess selected according to the c2d criteria, as well as the other YSOs cloud members and candidates from the previous surveys. Spectroscopic follow-ups, published in the literature, confirm the YSO nature of most of the selected candidates, supporting the reliability of the selection criteria.

The K-band luminosity function of L1630 N shows a broad peak between 10.5 and 12 mag., i.e.  $0.3\text{--}0.7 M_{\odot}$ , but steadily declines to the hydrogen-burning limit at  $K_S \approx 13$  mag. We predict a fraction of 28% young substellar objects, but we note that the expected contamination from field stars mimicking the colors of BDs is on the order of 50%, while in the stellar regime it is about 20%. Thus, the actual fraction of substellar objects in L1630 N may be  $\sim 20\%$ . The K-band luminosity function of L1630 N is remarkably similar to that of the Trapezium cluster.

The analysis of the SEDs shape shows that the L1630 N population is dominated by objects with active accretion, with only a minority being systems with passive disks. The disk/envelope fraction in the region of  $\sim 85\%$  is high in comparison with other star formation regions of similar age. The fraction of the Class I and Flat-spectrum sources (13% and 16%, respectively) in L1630 N and their respective phase lifetime (0.4 and 0.48 Myr, respectively) are consistent with the results for the c2d clouds (Evans et al., 2009).

We studied the spatial distribution and volume density of the 186 YSOs with the following results: we identify structures with volume densities higher than  $1 M_{\odot} \text{pc}^{-3}$  or  $10 M_{\odot} \text{pc}^{-3}$ . The loose clusters identified are L1630 N as a whole with a density of  $1 M_{\odot} \text{pc}^{-3}$  and NGC 2071 and NGC 2068 with a density of  $10 M_{\odot} \text{pc}^{-3}$ . The HH24-26 entity can be defined as a loose group with a density of  $10 M_{\odot} \text{pc}^{-3}$ .

The cloud mass determined from the VISTA extinction map is on the order of  $3865 M_{\odot}$  and the SFE of 2-2.8% is similar to previous estimates for the Orion A and B clouds and for the c2d clouds, but is much lower than the SFE measured in sub-clusters in the southern region L1630 S. The SFE of the sub-clusters in L1630 N is also comparably low. The different SFE in the northern and southern regions of L1630 might suggest different star formation mechanisms. The SFR is similar to that of the c2d clouds (Evans et al., 2009); we find that L1630 N is turning some  $75 M_{\odot}$  into YSOs every Myr. This is, however, lower than the average value measured for the Orion A and B clouds and the local SFR for the ONC and the Trapezium, but large variations of the SFR among the Orion sub-groupings are observed. Such variations disappear when considering the density of star formation  $\Sigma_{SFR}$ . The density of star formation  $\sim 2 M_{\odot} \text{Myr}^{-1} \text{pc}^{-2}$  and the gas surface density  $\sim 98 M_{\odot} \text{pc}^{-2}$  in L1630 N are in excellent agreement with previous determinations of galactic star-forming activity. At the level of the sub-clusters in L1630 N these quantities are also similar to those in the sub-clusters in other galactic star-forming regions. More than one-third of the cloud in L1630 N has a gas surface density above  $\Sigma_{th} \sim 129 M_{\odot} \text{pc}^{-2}$ . This may indicate that star formation in L1630 N is still on-going, which may explain the exceptionally high disk/envelope fraction in the region. The latter, however, needs to be confirmed in the future with deep observations tracing the complete population of young diskless sources.

*Acknowledgements.* We thank the anonymous referee for valuable comments which further improved the clarity of the paper. JMA acknowledges financial support from INAF under the program PRIN2013 "Disk jets and the dawn of planets". This research has made use of the SIMBAD database operated at CDS, Strasbourg, France. It also makes use of data products from the Two Micron All Sky Survey, which is a joint project of the University of Massachusetts and the Infrared Processing and Analysis Center/California Institute of Technology, funded by the National Aeronautics and Space Administration and the National Science Foundation. We greatly appreciate the work done by the UK-based



VISTA consortium who built and commissioned the VISTA telescope and camera.

## References

- Alcalá, J. M., Spezzi, L., Chapman, N., et al. 2008, *ApJ*, 676, 427
- Allard, F., Hauschildt, P. H., Alexander, D. R., Tamanai, A., & Schweitzer, A. 2001, *ApJ*, 556, 357
- Arnaboldi, M., Petr-Gotzens, M., Rejkuba, M., et al. 2010, *The Messenger*, 139, 6
- Baraffe, I., Chabrier, G., Allard, F., & Hauschildt, P. H. 1998, *A&A*, 337, 403
- Basri, G., & Reiners, A. 2006, *AJ*, 132, 663
- Beccari, G., Spezzi, L., De Marchi, G., et al. 2010, *ApJ*, 720, 1108
- Bessell, M. S. 1990, *PASP*, 102, 1181
- Bigiel, F., Leroy, A., Walter, F., et al. 2008, *AJ*, 136, 2846
- Briceño, C., Luhman, K. L., Hartmann, L., Stauffer, J. R., & Kirkpatrick, J. D. 2002, *ApJ*, 580, 317
- Briceño, C., Vivas, A. K., Hernández, J., et al. 2004, *ApJ*, 606, L123
- Cardelli, J. A., Clayton, G. C., & Mathis, J. S. 1989, *ApJ*, 345, 245
- Chabrier, G., Baraffe, I., Allard, F., & Hauschildt, P. 2000, *ApJ*, 542, 464
- Cieza, L. A., Schreiber, M. R., Romero, G. A., et al. 2010, *ApJ*, 712, 925
- Comerón, F. 2008, *Handbook of Star Forming Regions*, Volume II, 295
- Daemgen, S., Petr-Gotzens, M. G., Correia, S. 2013, *A&A*, 554, 43
- Dalton, G. B., Caldwell, M., Ward, A. K., et al. 2006, *Proc. SPIE*, 6269
- De Marchi, G., Panagia, N., Romaniello, M., et al. 2011, *ApJ*, 740, 11
- De Marchi, G., Paresce, F., Panagia, N., et al. 2011, *ApJ*, 739, 27
- Dullemond, C. P., & Dominik, C. 2005, *A&A*, 434, 971
- Dunham, M. M., Arce, H. G., Allen, L. E., et al. 2013, *AJ*, 145, 94
- Duquennoy, A., & Mayor, M. 1991, *Bioastronomy: The Search for Extraterrestrial Life – The Exploration Broadens*, 390, 39
- Emerson, J., McPherson, A., & Sutherland, W. 2006, *The Messenger*, 126, 41
- Evans, N. J., II. 2008, *Final Delivery of Data from the c2d Legacy Project: IRAC and MIPS (Pasadena: SSC)*
- Evans, N. J., II, Dunham, M. M., Jørgensen, J. K., et al. 2009, *ApJS*, 181, 321
- Fang, M., van Boekel, R., Wang, W., et al. 2009, *A&A*, 504, 461
- Fazio, G. G., Hora, J. L., Allen, L. E., et al. 2004, *ApJS*, 154, 10
- Fedele, D., van den Ancker, M. E., Henning, T., Jayawardhana, R., & Oliveira, J. M. 2010, *A&A*, 510, A72
- Federrath, C., & Klessen, R. S. 2013, *ApJ*, 763, 51
- Flaherty, K. M., & Muzerolle, J. 2008, *AJ*, 135, 966
- Gibb, A. G. 2008, *Handbook of Star Forming Regions*, Volume I, 693
- Greene, T. P., Wilking, B. A., Andre, P., Young, E. T., & Lada, C. J. 1994, *ApJ*, 434, 614
- Gutermuth, R. A., et al. 2005, *ApJ*, 632, 397
- Gutermuth, R. A., Pipher, J. L., Megeath, S. T., et al. 2011, *ApJ*, 739, 84
- Haisch, K. E., Jr., Lada, E. A., & Lada, C. J. 2001, *ApJ*, 553, L153
- Harvey, P., Merín, B., Huard, T. L., et al. 2007, *ApJ*, 663, 1149
- Harvey, P. M., Rebull, L. M., Brooke, T., et al. 2007, *ApJ*, 663, 1139
- Hatchell, J., Terebey, S., Huard, T., et al. 2012, *ApJ*, 754, 104
- Hauschildt, P. H., Allard, F., & Baron, E. 1999, *ApJ*, 512, 377
- Heiderman, A., Evans, N. J., II, Allen, L. E., Huard, T., & Heyer, M. 2010, *ApJ*, 723, 1019
- Hollenbach, D. J., Yorke, H. W., & Johnstone, D. 2000, *Protostars and Planets IV*, 401
- Hsu, W.-H., Hartmann, L., Allen, L., et al. 2012, *ApJ*, 752, 59
- Johansen, A., Youdin, A., & Mac Low, M.-M. 2009, *ApJ*, 704, L75
- Jørgensen, J. K., Johnstone, D., Kirk, H., et al. 2008, *ApJ*, 683, 822
- Kennicutt, R. C., Jr. 1998, *ApJ*, 498, 541
- Kennicutt, R. C., Jr., Calzetti, D., Walter, F., et al. 2007, *ApJ*, 671, 333
- Krumholz, M. R., McKee, C. F., & Tumlinson, J. 2009, *ApJ*, 693, 216
- Irwin, M. J., et al. 2004, *Proc. of SPIE*, 5493, 411
- Lada, C. J., & Wilking, B. A. 1984, *ApJ*, 287, 610
- Lada, C. J., Lada, E. A., Clemens, D. P., & Bally, J. 1994, *ApJ*, 429, 694
- Lada, C. J., Alves, J., & Lada, E. A. 1996, *AJ*, 111, 1964
- Lada, E. A., Evans, N. J. II, Falgarone, E. 1997, *ApJ*, 488, 286
- Lada, C. J., Muench, A. A., Haisch, K. E., Jr., et al. 2000, *AJ*, 120, 3162
- Lada, C. J., & Lada, E. A. 2003, *ARA&A*, 41, 57
- Lada, C. J. 2006, *ApJ*, 640, L63
- Lada, C. J., Lombardi, M., & Alves, J. F. 2010, *ApJ*, 724, 687
- Lee, H.-T., Chen, W. P., Zhang, Z.-W., & Hu, J.-Y. 2005, *ApJ*, 624, 808
- Linsky, J. L., Gagné, M., Mytyk, A., McCaughrean, M., & Andersen, M. 2007, *ApJ*, 654, 347
- Lombardi, M., & Alves, J. 2001, *A&A*, 377, 1023
- Lombardi, M. 2009, *A&A*, 493, 735
- Lonsdale, C. J., Smith, H. E., Rowan-Robinson, M., et al. 2003, *PASP*, 115, 89
- López Martí, B., Eislöffel, J., Scholz, A., & Mundt, R. 2004, *A&A*, 416, 555
- Luhman, K. L., & Rieke, G. H. 1999, *ApJ*, 525, 440
- Mason, B. D., Henry, T. J., Hartkopf, W. I., ten Brummelaar, T., & Soderblom, D. R. 1998, *AJ*, 116, 2975
- Megeath, S. T., Gutermuth, R., Muzerolle, J., et al. 2012, *AJ*, 144, 192
- Merín, B., Jørgensen, J., Spezzi, L., et al. 2008, *ApJS*, 177, 551
- Meyer, M. R., Calvet, N., & Hillenbrand, L. A. 1997, *AJ*, 114, 288
- Meyer, M. R., Flaherty, K., Levine, J. L., et al. 2008, *Handbook of Star Forming Regions*, Volume I, 662
- Miesch, M. S., & Bally, J. 1994, *ApJ*, 429, 645
- Muench, A. A., Lada, E. A., Lada, C. J., & Alves, J. 2002, *ApJ*, 573, 366
- Oliveira, I., Merín, B., Pontoppidan, K. M., et al. 2009, *ApJ*, 691, 672
- Palla, F., & Stahler, S. W. 1999, *ApJ*, 525, 772
- Petr-Gotzens, M., Alcalá, J. M., Briceño, C., et al. 2011, *The Messenger*, 145, 29
- Principe, D. A., Kastner, J. H., Grosso, N., et al. 2014, *ApJS*, 213, 4
- Rieke, G. H., Young, E. T., Engelbracht, C. W., et al. 2004, *ApJS*, 154, 25
- Robin, A. C., Reylé, C., Derrière, S., & Picaud, S. 2003, *A&A*, 409, 523
- Santiago, B. X., Gilmore, G., & Elson, R. A. W. 1996, *MNRAS*, 281, 871
- Scholz, A., Muzic, K., Geers, V., et al. 2012, *ApJ*, 744, 6
- Sicilia-Aguilar, A., Hartmann, L., Calvet, N., et al. 2006, *ApJ*, 638, 89
- Sicilia-Aguilar, A., et al. 2013, *A&A*, submitted
- Skinner, S. L., Simmons, A. E., Audard, & M. Güdel, M. 2007, *ApJ*, 658, 1144
- Skrutskie, M. F., Cutri, R. M., Stiening, R., et al. 2006, *AJ*, 131, 1163
- Spezzi, L., Alcalá, J. M., Frasca, A., Covino, E., & Gandolfi, D. 2007, *A&A*, 470, 281
- Spezzi, L., Alcalá, J. M., Covino, E., et al. 2008, *ApJ*, 680, 1295
- Spezzi, L., Pagano, I., Marino, G., et al. 2009, *A&A*, 499, 541
- Spezzi, L., Vernazza, P., Merín, B., et al. 2011, *ApJ*, 730, 65
- Spezzi, L., de Marchi, G., Panagia, N., Sicilia-Aguilar, A., & Ercolano, B. 2012, *MNRAS*, 421, 78
- Stutz, A. M., Tobin, J. J., Stanke, Th., et al. 2013, *AJ*, 767, 36
- Surace, J. A., Shupe, D. L., Fang, F., et al. 2004, *VizieR Online Data Catalog*, 2255, 0
- Wainscoat, R. J., Cohen, M., Volk, K., Walker, H. J., & Schwartz, D. E. 1992, *ApJS*, 83, 111
- Watson, M. G., Schröder, A. C., Fyfe, D., et al. 2009, *A&A*, 493, 339
- White, R. J., Basri, G. 2003, *ApJ*, 582, 1109
- Whitworth, A., Bate, M. R., Nordlund, Å., Reipurth, B., & Zinnecker, H. 2007, *Protostars and Planets V*, 459
- Wu, J., Evans, N. J., II, Shirley, Y. L., & Knez, C. 2010, *ApJS*, 188, 313
- Zacharias, N., Finch, C. T., Girard, T. M., et al. 2013, *AJ*, 145, 44

## Appendix A: Theoretical isochrones in the VISTA photometric system

Theoretical isochrones for low-mass stars and BDs down to  $0.001 M_{\odot}$  are provided by Baraffe et al. (1998) and Chabrier et al. (2000) in the Cousins photometric system (Bessell, 1990), and are the most commonly used for very low-mass stellar population studies. In particular, they are extensively used to select PMS star and young BD candidates on the basis of color-magnitude diagrams (CMDs). Since the transmission curves of the VISTA filters are very different from the Cousins ones, we transformed these isochrones into the specific VISTA photometric system. In this way, we make available to the community a valuable tool to be used in extensive VISTA-based searches for very low-mass stars and BDs in other stars forming regions.

The procedure adopted to perform the conversion of the evolutionary models from one system to another has been already described in detail in Spezzi et al. (2007) (appendix B). The expected flux ( $f_{\Delta\lambda}$ ) at the stellar surface in the VISTA pass-bands were determined by integrating the synthetic low-resolution spectra for low-mass stars by Hauschildt et al. (1999), calculated with their NextGen model-atmosphere code, under the filter transmission curves<sup>8</sup> (see Fig. A.1, upper panel). For simulating very cool objects (i.e.  $T_{\text{eff}} < 3000$  K) we used the AMES-Dusty and AMES-Cond atmosphere models by Allard et al. (2001), which take into account the formation of condensed

<sup>8</sup> Available at <http://apm49.ast.cam.ac.uk/surveys-projects/vista/technical/filterset>

species significantly modifying the atmospheric structure<sup>9</sup>. The expected flux  $f_{\Delta\lambda}$  was then converted to absolute magnitudes using the following equation:

$$m_{\Delta\lambda} = -2.5 \cdot \log_{10} \left( f_{\Delta\lambda} \cdot \frac{R_{\star}}{d} \right) + C_{\Delta\lambda} \quad (\text{A.1})$$

where  $d=10$  pc,  $R_{\star}$  is the stellar radius expected for PMS objects and computed from the theoretical PMS evolutionary tracks by Baraffe et al. (1998) for low-mass stars and those by Chabrier et al. (2000) for sub-stellar objects (i.e.  $M \lesssim 0.1 M_{\odot}$ ), and  $C_{\Delta\lambda}$  is the absolute calibration constant of the VISTA photometric system, tied to the Earth flux of an A0-type star with magnitude  $V=0$ <sup>10</sup>. In Figure A.1 (lower panel) we show, as an example, the theoretical 1, 5 and 10 Myr isochrones and the ZAMS (5 Gyr) on the  $M_J$  vs.  $J - K_S$  CMD and make them publicly available in Table A.1, where we also give isochrones for 50 Myr and 100 Myr.

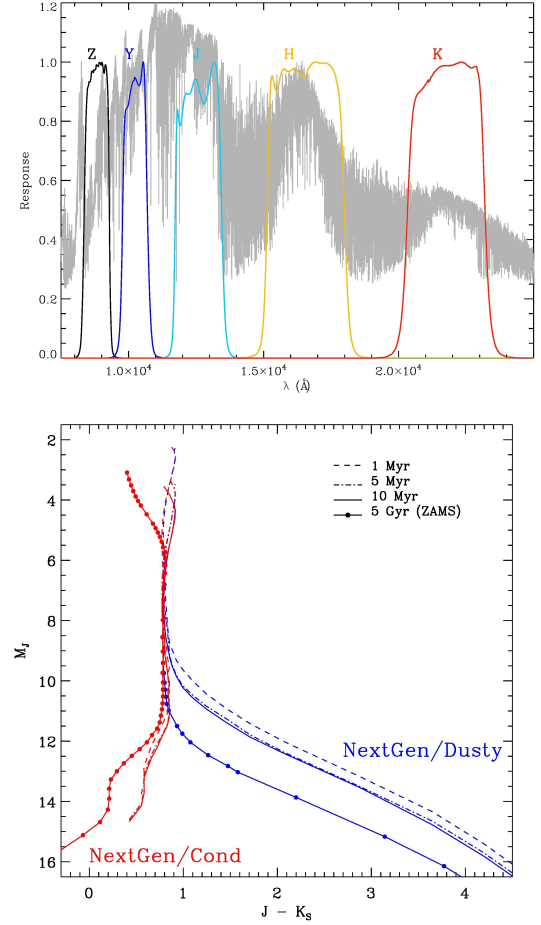


**Fig. A.1.** Upper panel: The ZYJHK<sub>S</sub> VISTA transmission bands. An example of a normalized NextGen spectrum (Hauschildt et al., 1999) with  $T_{\text{eff}} = 2500$  K is overplotted. Lower panel: Theoretical  $M_J$  vs.  $J - K_S$  diagram. The isochrones, shifted to the distance of 10 pc (i.e., absolute magnitudes), are in the VISTA photometric system. Different curve-styles correspond to different ages, as indicated in the legend. We plot in blue the isochrones computed using the NextGen/AMES-Dusty atmospheric models, and in red those computed using the NextGen/AMES-Cond models.

<sup>9</sup> While in the AMES-Dusty models the condensed species are included both in the equation of state and in the opacity, taking into account dust scattering and absorption, in the AMES-Cond models the opacity of these condensates is ignored, in order to mimic a rapid gravitational settling of all grains below the photosphere

<sup>10</sup> <http://apm49.ast.cam.ac.uk/surveys-projects/vista/technical/photometricproperties>

**Table A.1.** Theoretical isochrones from Baraffe et al. (1998) and Chabrier et al. (2000) converted into the VISTA photometric system.

Mass ( $M_{\odot}$ )	$T_{eff}$ (K)	Z	Y	J	H	$K_S$	Z	Y	J	H	$K_S$
NextGen/AMES-Dusty						NextGen/AMES-Cond					
1 Myrs											
0.002	1300	20.899	18.949	16.523	13.923	11.824	15.192	13.621	12.496	12.326	11.875
0.002	1400	19.306	17.576	15.410	13.066	11.211	14.251	13.354	12.133	11.904	11.470
0.003	1500	17.958	16.376	14.336	12.237	10.691	13.900	13.042	11.777	11.516	11.055
0.003	1600	16.643	15.123	13.181	11.525	10.300	13.945	12.610	11.426	11.147	10.646
0.004	1700	15.110	13.702	12.031	10.881	9.949	13.754	12.172	11.105	10.812	10.278
0.004	1800	14.359	12.961	11.422	10.511	9.710	13.320	11.773	10.788	10.490	9.941
0.005	1900	13.659	12.310	10.920	10.173	9.463	12.877	11.365	10.482	10.179	9.629
0.006	2000	12.951	11.666	10.427	9.813	9.184	12.420	11.142	10.147	9.837	9.302
0.007	2100	12.354	11.129	10.006	9.475	8.904	11.928	10.960	9.818	9.497	8.984
0.009	2200	11.794	10.636	9.614	9.143	8.623	11.459	10.588	9.531	9.165	8.677
0.011	2300	11.330	10.254	9.319	8.877	8.393	11.091	10.258	9.274	8.904	8.440
0.014	2400	10.816	9.826	8.966	8.541	8.085	10.646	9.867	8.951	8.573	8.128
0.018	2500	10.467	9.568	8.768	8.347	7.913	10.329	9.603	8.753	8.367	7.945
0.024	2600	10.001	9.187	8.436	8.012	7.596	9.893	9.215	8.417	8.025	7.623
0.030	2700	9.386	8.649	7.936	7.507	7.109	9.319	8.691	7.935	7.524	7.129
0.041	2800	8.725	8.050	7.366	6.932	6.552	8.665	8.079	7.359	6.939	6.564
0.062	2900	7.850	7.219	6.556	6.117	5.754	7.766	7.216	6.526	6.097	5.743
0.101	3000	6.846	6.264	5.624	5.173	4.834	6.781	6.262	5.597	5.152	4.822
0.142	3100	6.151	5.613	4.991	4.517	4.205	6.113	5.623	4.977	4.505	4.203
0.207	3200	5.591	5.088	4.482	3.971	3.685	5.565	5.099	4.470	3.958	3.683
0.326	3300	5.075	4.603	4.009	3.454	3.190	5.055	4.614	3.998	3.435	3.185
0.465	3400	4.626	4.180	3.595	2.992	2.750	4.608	4.189	3.581	2.960	2.736
0.590	3500	4.286	3.861	3.279	2.627	2.410	4.275	3.869	3.267	2.595	2.396
0.709	3600	4.008	3.603	3.022	2.324	2.134	4.005	3.618	3.017	2.305	2.126
0.843	3700	3.752	3.369	2.792	2.064	1.887	3.744	3.380	2.785	2.045	1.875
0.985	3800	3.526	3.168	2.601	1.858	1.688	3.515	3.178	2.595	1.845	1.678
1.151	3900	3.258	2.927	2.375	1.637	1.471	3.242	2.928	2.364	1.625	1.463
1.214	4000	3.120	2.832	2.278	1.539	1.367	3.089	2.799	2.252	1.532	1.375
5 Myrs											
0.002	900	29.734	26.453	22.394	18.219	15.123	17.537	15.510	14.602	14.666	14.177
0.004	1300	21.184	19.234	16.808	14.208	12.109	15.477	13.906	12.781	12.611	12.160
0.005	1400	19.603	17.874	15.707	13.363	11.509	14.549	13.651	12.431	12.202	11.768
0.006	1500	18.271	16.689	14.649	12.550	11.004	14.213	13.355	12.090	11.829	11.368
0.006	1600	16.974	15.454	13.512	11.856	10.630	14.276	12.941	11.757	11.478	10.976
0.007	1700	15.462	14.055	12.383	11.234	10.302	14.106	12.525	11.458	11.165	10.630
0.008	1800	14.730	13.332	11.793	10.881	10.081	13.691	12.144	11.159	10.861	10.311
0.010	1900	13.994	12.645	11.255	10.508	9.798	13.212	11.700	10.817	10.514	9.964
0.012	2000	13.359	12.075	10.836	10.222	9.593	12.828	11.551	10.555	10.246	9.711
0.013	2100	12.827	11.603	10.480	9.948	9.378	12.402	11.433	10.292	9.971	9.458
0.014	2200	12.329	11.172	10.150	9.679	9.159	11.995	11.124	10.066	9.701	9.213
0.016	2300	11.828	10.752	9.817	9.376	8.891	11.589	10.757	9.772	9.402	8.938
0.018	2400	11.312	10.322	9.461	9.037	8.581	11.141	10.362	9.447	9.068	8.624
0.020	2500	10.845	9.946	9.146	8.725	8.291	10.707	9.982	9.131	8.746	8.323
0.025	2600	10.200	9.386	8.634	8.210	7.794	10.092	9.414	8.615	8.224	7.822
0.030	2700	9.630	8.893	8.180	7.751	7.353	9.563	8.935	8.179	7.768	7.373
0.040	2800	9.181	8.506	7.822	7.388	7.008	9.121	8.534	7.815	7.395	7.020
0.053	2900	8.911	8.280	7.617	7.178	6.815	8.827	8.277	7.587	7.158	6.803
0.076	3000	8.423	7.841	7.200	6.750	6.410	8.357	7.839	7.173	6.728	6.399
0.113	3100	7.853	7.314	6.693	6.218	5.907	7.815	7.324	6.678	6.207	5.904
0.177	3200	7.185	6.682	6.076	5.565	5.279	7.159	6.693	6.064	5.552	5.277
0.261	3300	6.599	6.127	5.533	4.978	4.715	6.579	6.138	5.522	4.959	4.709
0.348	3400	6.152	5.706	5.121	4.519	4.276	6.135	5.715	5.107	4.487	4.263
0.456	3500	5.740	5.315	4.733	4.081	3.864	5.729	5.323	4.721	4.049	3.850
0.588	3600	5.342	4.937	4.356	3.658	3.468	5.339	4.952	4.351	3.639	3.460
0.735	3700	5.000	4.617	4.040	3.312	3.135	4.991	4.627	4.033	3.293	3.123
0.879	3800	4.727	4.370	3.803	3.059	2.889	4.717	4.379	3.797	3.046	2.880
1.006	3900	4.481	4.150	3.598	2.860	2.694	4.465	4.151	3.587	2.848	2.686
1.070	4000	4.313	4.025	3.471	2.732	2.560	4.282	3.992	3.444	2.725	2.568
10 Myrs											
0.003	900	29.799	26.519	22.460	18.285	15.189	17.603	15.576	14.668	14.732	14.243
0.006	1300	21.280	19.330	16.904	14.304	12.205	15.573	14.002	12.877	12.707	12.256
0.007	1400	19.718	17.988	15.822	13.478	11.623	14.663	13.766	12.545	12.317	11.882
0.008	1500	18.392	16.810	14.770	12.671	11.125	14.334	13.476	12.211	11.950	11.489
0.010	1600	17.006	15.486	13.544	11.888	10.663	14.308	12.973	11.789	11.510	11.008
0.011	1700	15.501	14.094	12.422	11.273	10.341	14.145	12.564	11.497	11.203	10.669
0.012	1800	14.807	13.408	11.870	10.958	10.157	13.767	12.221	11.236	10.937	10.388
0.013	1900	14.121	12.772	11.382	10.635	9.925	13.338	11.827	10.944	10.641	10.091
0.014	2000	13.452	12.168	10.929	10.315	9.686	12.921	11.644	10.649	10.339	9.804
0.014	2100	12.914	11.689	10.566	10.035	9.465	12.489	11.520	10.379	10.057	9.544
0.016	2200	12.391	11.234	10.212	9.740	9.220	12.057	11.186	10.128	9.762	9.274

Continued on Next Page...

Mass ( $M_{\odot}$ )	$T_{eff}$ (K)	Z	Y	J	H	$K_S$	Z	Y	J	H	$K_S$
0.017	2300	11.856	10.780	9.845	9.403	8.919	11.617	10.784	9.800	9.430	8.966
0.019	2400	11.367	10.377	9.517	9.092	8.636	11.197	10.418	9.502	9.124	8.680
0.021	2500	10.926	10.027	9.227	8.806	8.372	10.788	10.062	9.212	8.826	8.404
0.026	2600	10.536	9.722	8.971	8.547	8.131	10.428	9.750	8.952	8.560	8.158
0.034	2700	10.212	9.475	8.762	8.333	7.935	10.145	9.517	8.761	8.350	7.955
0.045	2800	9.906	9.230	8.547	8.113	7.733	9.845	9.259	8.540	8.120	7.745
0.059	2900	9.514	8.884	8.220	7.782	7.418	9.430	8.880	8.190	7.761	7.407
0.081	3000	8.994	8.412	7.771	7.321	6.981	8.928	8.410	7.744	7.299	6.970
0.105	3100	8.514	7.976	7.354	6.880	6.568	8.476	7.986	7.340	6.868	6.566
0.160	3200	7.875	7.372	6.766	6.255	5.969	7.849	7.383	6.754	6.242	5.967
0.247	3300	7.207	6.735	6.141	5.586	5.323	7.187	6.746	6.130	5.567	5.317
0.354	3400	6.649	6.203	5.618	5.015	4.773	6.631	6.212	5.603	4.983	4.759
0.447	3500	6.279	5.854	5.272	4.620	4.403	6.267	5.862	5.260	4.588	4.389
0.549	3600	5.931	5.526	4.945	4.247	4.056	5.928	5.541	4.940	4.227	4.049
0.674	3700	5.603	5.219	4.643	3.915	3.738	5.594	5.230	4.636	3.896	3.726
0.806	3800	5.292	4.934	4.367	3.623	3.454	5.281	4.943	4.361	3.610	3.444
0.916	3900	5.039	4.708	4.157	3.418	3.253	5.023	4.710	4.145	3.406	3.244
1.000	4000	4.851	4.563	4.009	3.270	3.098	4.820	4.529	3.982	3.263	3.106
50 Myrs											
0.008	1000	26.796	24.021	20.576	16.967	14.265	17.196	15.415	14.245	14.536	14.312
0.010	1100	24.515	22.092	19.076	15.874	13.421	16.609	14.773	13.612	13.853	13.497
0.011	1300	21.467	19.485	17.010	14.339	12.215	15.558	13.902	12.789	12.933	12.577
0.012	1500	18.600	17.008	14.980	12.808	11.207	14.785	13.215	12.105	12.125	11.875
0.013	1600	17.366	15.899	13.973	12.121	10.831	14.459	12.909	11.803	11.746	11.511
0.014	1700	15.810	14.427	12.659	11.367	10.459	14.095	12.577	11.527	11.409	11.161
0.015	1800	14.695	13.383	11.806	10.894	10.227	13.739	12.279	11.267	11.097	10.816
0.023	1900	14.656	13.365	11.850	10.998	10.377	13.662	12.228	11.289	11.077	10.753
0.025	2000	14.150	12.897	11.498	10.777	10.233	13.329	12.064	11.072	10.821	10.460
0.028	2100	13.499	12.336	11.108	10.512	10.033	12.973	11.987	10.867	10.582	10.200
0.030	2200	13.077	11.980	10.858	10.317	9.870	12.644	11.814	10.692	10.366	9.971
0.034	2300	12.666	11.640	10.613	10.106	9.680	12.323	11.565	10.494	10.140	9.745
0.041	2500	11.875	11.011	10.148	9.686	9.302	11.688	11.061	10.108	9.712	9.335
0.047	2600	11.496	10.713	9.913	9.455	9.087	11.358	10.781	9.889	9.475	9.111
0.054	2700	11.138	10.431	9.682	9.222	8.866	11.036	10.501	9.668	9.238	8.885
0.064	2800	10.739	10.101	9.396	8.933	8.589	10.670	10.171	9.390	8.947	8.607
0.078	2900	10.332	9.752	9.082	8.614	8.282	10.278	9.810	9.076	8.622	8.294
0.094	3000	9.988	9.457	8.818	8.343	8.025	9.945	9.503	8.811	8.347	8.031
0.112	3100	9.661	9.172	8.558	8.078	7.773	9.641	9.221	8.566	8.089	7.780
0.146	3200	9.213	8.763	8.171	7.681	7.381	9.185	8.787	8.162	7.676	7.381
0.198	3300	8.675	8.252	7.681	7.182	6.903	8.662	8.281	7.685	7.189	6.907
0.287	3400	8.099	7.706	7.154	6.641	6.366	8.080	7.715	7.145	6.633	6.363
0.399	3500	7.548	7.179	6.641	6.113	5.849	7.532	7.182	6.634	6.104	5.844
0.517	3600	7.064	6.716	6.193	5.649	5.393	7.049	6.718	6.184	5.636	5.386
0.588	3700	6.743	6.414	5.903	5.343	5.100	6.732	6.419	5.896	5.331	5.091
0.633	3800	6.503	6.192	5.692	5.119	4.885	6.490	6.192	5.679	5.095	4.870
0.669	3900	6.271	5.973	5.481	4.887	4.674	6.259	5.975	5.470	4.866	4.659
0.703	4000	6.059	5.777	5.291	4.685	4.489	6.046	5.775	5.275	4.653	4.466
100 Myrs											
0.010	900	29.315	26.071	22.068	18.154	15.116	17.558	15.865	14.757	15.040	15.076
0.010	1000	26.709	23.933	20.489	16.879	14.178	17.109	15.328	14.158	14.449	14.225
0.011	1100	24.561	22.138	19.122	15.920	13.467	16.655	14.820	13.658	13.900	13.543
0.012	1300	21.506	19.523	17.049	14.377	12.253	15.596	13.940	12.827	12.971	12.615
0.021	1500	18.931	17.339	15.311	13.139	11.537	15.116	13.546	12.436	12.456	12.206
0.024	1600	17.742	16.274	14.349	12.497	11.207	14.835	13.285	12.179	12.122	11.887
0.026	1700	16.230	14.847	13.079	11.787	10.880	14.515	12.998	11.948	11.829	11.581
0.028	1800	15.158	13.847	12.269	11.358	10.691	14.203	12.743	11.731	11.561	11.280
0.031	1900	14.897	13.605	12.091	11.238	10.617	13.903	12.468	11.530	11.317	10.994
0.033	2000	14.391	13.138	11.738	11.018	10.474	13.570	12.305	11.313	11.062	10.701
0.036	2100	13.740	12.577	11.349	10.753	10.274	13.214	12.228	11.108	10.823	10.441
0.039	2200	13.319	12.221	11.099	10.558	10.111	12.886	12.056	10.934	10.608	10.212
0.043	2300	12.918	11.892	10.865	10.358	9.932	12.575	11.817	10.745	10.392	9.997
0.051	2500	12.135	11.271	10.408	9.946	9.562	11.948	11.321	10.368	9.972	9.595
0.057	2600	11.773	10.990	10.190	9.732	9.364	11.635	11.058	10.167	9.753	9.388
0.064	2700	11.425	10.717	9.968	9.508	9.152	11.323	10.787	9.954	9.524	9.171
0.073	2800	11.063	10.425	9.721	9.257	8.914	10.995	10.495	9.715	9.271	8.932
0.087	2900	10.698	10.118	9.448	8.979	8.648	10.644	10.175	9.442	8.988	8.660
0.104	3000	10.375	9.844	9.204	8.730	8.411	10.332	9.890	9.198	8.734	8.418
0.123	3100	10.040	9.551	8.937	8.457	8.152	10.020	9.600	8.945	8.468	8.159
0.150	3200	9.664	9.214	8.623	8.133	7.833	9.636	9.238	8.614	8.128	7.832
0.201	3300	9.155	8.733	8.162	7.662	7.384	9.142	8.761	8.166	7.669	7.387
0.277	3400	8.611	8.219	7.666	7.153	6.879	8.592	8.228	7.658	7.146	6.875
0.377	3500	8.068	7.698	7.161	6.632	6.369	8.051	7.701	7.153	6.624	6.364
0.461	3600	7.595	7.247	6.724	6.180	5.924	7.580	7.248	6.714	6.167	5.916
0.514	3700	7.248	6.919	6.408	5.848	5.605	7.237	6.924	6.401	5.836	5.596
0.548	3800	6.999	6.688	6.188	5.615	5.381	6.986	6.688	6.175	5.591	5.366

Continued on Next Page...

Mass ( $M_{\odot}$ )	$T_{eff}$ (K)	Z	Y	J	H	$K_S$	Z	Y	J	H	$K_S$
0.579	3900	6.772	6.475	5.982	5.388	5.175	6.760	6.476	5.971	5.368	5.160
0.603	4000	6.580	6.298	5.813	5.207	5.010	6.567	6.297	5.796	5.174	4.988
5 Gyrs (ZAMS)											
0.050	900	30.203	26.959	22.956	19.042	16.004	18.446	16.753	15.645	15.928	15.964
0.055	1000	27.670	24.895	21.451	17.841	15.140	18.071	16.289	15.119	15.410	15.187
0.060	1100	25.589	23.166	20.150	16.948	14.494	17.683	15.847	14.685	14.927	14.571
0.064	1300	22.585	20.603	18.128	15.457	13.333	16.676	15.020	13.907	14.051	13.695
0.068	1500	19.766	18.175	16.146	13.975	12.373	15.951	14.381	13.272	13.292	13.042
0.070	1600	18.561	17.094	15.169	13.317	12.026	15.654	14.105	12.999	12.941	12.706
0.071	1700	17.018	15.636	13.867	12.576	11.668	15.303	13.786	12.736	12.617	12.369
0.073	1800	15.917	14.605	13.028	12.116	11.449	14.961	13.501	12.489	12.319	12.038
0.074	1900	15.631	14.339	12.825	11.972	11.351	14.637	13.202	12.264	12.051	11.728
0.075	2000	15.119	13.866	12.466	11.746	11.202	14.298	13.033	12.041	11.790	11.429
0.077	2100	14.429	13.266	12.038	11.441	10.963	13.903	12.917	11.797	11.512	11.130
0.078	2200	13.970	12.872	11.751	11.210	10.762	13.537	12.707	11.585	11.259	10.864
0.080	2300	13.551	12.525	11.498	10.991	10.565	13.208	12.450	11.379	11.025	10.630
0.086	2500	12.709	11.845	10.982	10.520	10.137	12.522	11.895	10.942	10.546	10.169
0.089	2600	12.350	11.567	10.766	10.309	9.941	12.211	11.635	10.743	10.329	9.964
0.095	2700	11.989	11.281	10.532	10.072	9.716	11.887	11.351	10.518	10.088	9.735
0.101	2800	11.637	11.000	10.295	9.831	9.488	11.569	11.069	10.289	9.846	9.506
0.108	2900	11.307	10.727	10.058	9.589	9.257	11.253	10.785	10.052	9.597	9.269
0.122	3000	10.914	10.382	9.743	9.268	8.950	10.870	10.428	9.736	9.272	8.956
0.139	3100	10.506	10.017	9.403	8.923	8.618	10.486	10.066	9.411	8.934	8.625
0.165	3200	10.075	9.625	9.034	8.544	8.244	10.047	9.649	9.025	8.539	8.243
0.205	3300	9.542	9.120	8.549	8.049	7.771	9.529	9.148	8.553	8.056	7.774
0.270	3400	8.937	8.544	7.992	7.479	7.205	8.918	8.553	7.983	7.471	7.201
0.377	3500	8.215	7.845	7.308	6.779	6.516	8.198	7.848	7.300	6.771	6.511
0.463	3600	7.673	7.325	6.802	6.258	6.002	7.658	7.327	6.793	6.245	5.995
0.523	3700	7.274	6.944	6.434	5.874	5.630	7.263	6.949	6.427	5.861	5.622
0.568	3800	6.981	6.670	6.170	5.597	5.363	6.968	6.670	6.157	5.573	5.348
0.602	3900	6.731	6.434	5.941	5.347	5.134	6.719	6.436	5.930	5.327	5.120
0.631	4000	6.517	6.234	5.749	5.143	4.946	6.503	6.233	5.732	5.110	4.924



**Table A.2.** VISTA and *Spitzer* observed magnitudes for the YSO candidates in L1630 N. When the photometric errors are not reported, the corresponding magnitude is an upper limit to the actual brightness of the object. The “–” symbol indicates that the object has not been detected in the given VISTA pass-band. The Lada classes marked with “?” are uncertain because the corresponding  $K_S$  magnitude is uncertain (i.e. photometric contamination, large photometric errors, object truncated or partially saturated, etc.). Column 3 specifies whether the object has been previously identified by Flaherty & Muzerolle (2008) (F08) and/or Fang et al. (2009) (FA09).

ID	Name/Position (VISTAomsJ)	Previous Identification	Lada Class	Z	Y	J	H	K <sub>S</sub>	IRAC 3.6μm	IRAC 4.5μm	IRAC 5.8μm	IRAC 8μm	MIPS 24μm
1	054803.999+000341.11		III?	10.635	10.153	8.723	8.467	7.167	6.526 ± 0.002	6.559 ± 0.001	6.353 ± 0.001	6.178 ± 0.001	5.251 ± 0.009
2	054713.848+000016.92	F08/FA09	II?	11.748	11.129	10.129	9.310	8.728	8.233 ± 0.003	7.824 ± 0.003	7.599 ± 0.001	7.022 ± 0.001	4.531 ± 0.014
3	054619.061+000329.56	F08/FA09	Flat	12.530	11.655	10.414	11.383 ± 0.001	10.029 ± 0.001	6.542 ± 0.002	6.005 ± 0.002	5.597 ± 0.003	4.937 ± 0.002	2.231 ± 0.013
4	054811.880-002157.46		III?	11.994	11.216	10.427	9.418	9.016	8.981 ± 0.005	8.972 ± 0.002	8.841 ± 0.003	8.758 ± 0.004	8.593 ± 0.145
5	054619.470-000519.97	F08/FA09	II?	11.986	–	10.602	9.668	9.127	7.960 ± 0.003	7.497 ± 0.002	7.151 ± 0.002	6.052 ± 0.003	3.002 ± 0.010
6	054705.993+003208.41	F08/FA09	II?	13.361 ± 0.001	12.570	10.705	10.013	9.275	8.095 ± 0.003	7.578 ± 0.003	7.249 ± 0.001	6.527 ± 0.001	3.101 ± 0.009
7	054604.671+000458.01	F08/FA09	II?	11.511	11.854	10.926	9.954	9.301	8.296 ± 0.003	7.887 ± 0.004	7.472 ± 0.001	6.692 ± 0.001	3.796 ± 0.015
8	054618.893-000538.11	F08/FA09	II?	12.560	11.911	11.129	10.291	9.875	8.945 ± 0.005	8.654 ± 0.001	8.183 ± 0.002	7.568 ± 0.002	5.730 ± 0.013
9	054707.262+001932.16	F08/FA09	Flat	12.181	11.280	11.146 ± 0.001	11.039 ± 0.001	10.135 ± 0.001	7.400 ± 0.002	6.883 ± 0.002	6.429 ± 0.001	5.582 ± 0.004	3.292 ± 0.016
10	054658.138+000538.33	F08/FA09	II?	12.960	12.162	11.210	10.256	9.847	9.395 ± 0.005	9.204 ± 0.001	8.943 ± 0.007	8.464 ± 0.022	5.066 ± 0.012
11	054714.110+000907.34	F08	I	12.548 ± 0.001	12.254 ± 0.001	11.280 ± 0.001	11.142 ± 0.001	10.877 ± 0.001	6.685 ± 0.001	5.703 ± 0.001	5.074 ± 0.002	3.974 ± 0.001	1.057 ± 0.007
12	054706.960+000047.66	F08/FA09	II?	12.420	11.836	11.316	10.602	10.353	9.818 ± 0.001	9.582 ± 0.001	9.219 ± 0.003	8.170 ± 0.003	4.878 ± 0.014
13	054609.261+001332.70	F08/FA09	II?	12.649	11.850	11.332	10.134	9.765	8.947 ± 0.004	8.603 ± 0.002	8.083 ± 0.001	7.468 ± 0.002	4.358 ± 0.012
14	054607.884-001156.83	F08/FA09	III?	12.387 ± 0.001	12.101 ± 0.001	11.352 ± 0.001	8.356	8.195	8.106 ± 0.003	7.974 ± 0.003	7.720 ± 0.002	7.293 ± 0.001	5.116 ± 0.006
15	054637.061+000121.86	F08/FA09	II?	13.273 ± 0.001	12.312	11.409	11.147 ± 0.001	9.621	8.226 ± 0.003	7.791 ± 0.003	7.426 ± 0.003	6.700 ± 0.007	3.126 ± 0.006
16	054622.436-000852.58	F08/FA09	II?	12.574	12.150	11.414	11.333 ± 0.001	10.281	9.542 ± 0.001	9.364 ± 0.001	9.177 ± 0.003	8.491 ± 0.002	4.797 ± 0.011
17	054611.869+003225.91	F08/FA09	II	12.656 ± 0.001	12.424 ± 0.001	11.457 ± 0.001	11.444 ± 0.001	10.486 ± 0.001	8.680 ± 0.004	8.580 ± 0.002	8.382 ± 0.002	8.142 ± 0.002	4.348 ± 0.015
18	054545.588+002556.96		II	15.487 ± 0.002	13.431 ± 0.001	11.537 ± 0.001	11.628 ± 0.001	10.952 ± 0.001	6.687 ± 0.002	6.539 ± 0.002	6.238 ± 0.001	6.091 ± 0.004	5.363 ± 0.014
19	054645.813+001702.51		II	12.819 ± 0.001	12.552 ± 0.001	11.543 ± 0.001	11.320 ± 0.001	10.411 ± 0.001	8.759 ± 0.004	8.376 ± 0.004	7.994 ± 0.002	7.385 ± 0.002	4.459 ± 0.017
20	054650.215+000439.61		II?	12.879	12.386	11.550	10.745	10.173	9.437 ± 0.002	8.810 ± 0.001	8.398 ± 0.009	7.423 ± 0.024	3.763 ± 0.016
21	054631.053+002533.74	F08	Flat	13.142	12.503	11.559	11.271 ± 0.001	10.343 ± 0.001	8.445 ± 0.004	7.887 ± 0.003	7.389 ± 0.002	6.441 ± 0.001	3.428 ± 0.010
22	054644.083+001803.17	F08/FA09	II	13.085 ± 0.001	12.574 ± 0.001	11.587	11.323 ± 0.001	10.517 ± 0.001	9.433 ± 0.005	9.130 ± 0.002	8.717 ± 0.002	8.049 ± 0.003	5.857 ± 0.021
23	054557.384+002022.20	F08/FA09	II?	13.172 ± 0.001	12.790 ± 0.001	11.837	11.535 ± 0.001	10.509	9.291 ± 0.001	9.009 ± 0.002	8.807 ± 0.003	8.099 ± 0.002	5.007 ± 0.014
24	054541.948-001205.26	F08/FA09	II	13.035 ± 0.001	12.845 ± 0.001	11.986 ± 0.001	11.577 ± 0.001	11.071 ± 0.002	10.862 ± 0.002	10.947 ± 0.003	10.741 ± 0.011	10.667 ± 0.011	6.498 ± 0.040
25	054634.539+000643.49	F08/FA09	II?	14.277 ± 0.001	13.273 ± 0.001	12.007 ± 0.001	11.238 ± 0.001	9.559	8.736 ± 0.004	8.266 ± 0.004	7.901 ± 0.003	7.230 ± 0.009	4.990 ± 0.009
26	054600.178+000307.09	F08/FA09	II?	13.300	12.687	12.015	11.309	10.957	10.425 ± 0.002	10.110 ± 0.002	9.725 ± 0.004	8.932 ± 0.003	5.652 ± 0.016
27	054645.040+000533.90	FA09	II?	13.912 ± 0.001	12.812	12.025 ± 0.001	10.753	10.218	9.427 ± 0.004	8.972 ± 0.004	8.530 ± 0.006	7.707 ± 0.017	4.372 ± 0.028
28	054646.871+000907.67	F08/FA09	II?	13.457 ± 0.001	13.171 ± 0.001	12.026 ± 0.001	11.116	10.224	9.614 ± 0.002	9.073 ± 0.001	8.713 ± 0.011	7.708 ± 0.025	4.351 ± 0.014
29	054618.296+000657.82	F08/FA09	II?	13.710 ± 0.001	12.950	12.091 ± 0.001	11.511 ± 0.001	10.524	9.534 ± 0.002	9.085 ± 0.001	8.604 ± 0.004	7.690 ± 0.008	4.916 ± 0.018
30	054556.316+000708.58	F08/FA09	II	13.295 ± 0.001	12.691	12.140 ± 0.001	11.410	11.093 ± 0.002	10.168 ± 0.002	9.921 ± 0.002	9.642 ± 0.004	9.241 ± 0.004	5.398 ± 0.013
31	054626.649+003107.43	F08/FA09	II?	13.921 ± 0.001	13.391 ± 0.001	12.182 ± 0.001	11.232	10.463	9.545 ± 0.001	9.163 ± 0.002	8.819 ± 0.002	8.142 ± 0.002	5.883 ± 0.014
32	054647.287+000407.10		II?	14.186 ± 0.001	13.930 ± 0.001	12.229 ± 0.001	10.482	9.556	8.664 ± 0.004	8.176 ± 0.004	7.773 ± 0.004	7.061 ± 0.014	4.180 ± 0.010
33	054544.374+002258.30	F08/FA09	II?	13.566 ± 0.001	12.965 ± 0.001	12.242 ± 0.001	11.157	10.615	9.387 ± 0.001	8.943 ± 0.001	8.667 ± 0.003	8.006 ± 0.002	5.265 ± 0.011
34	054633.285+000251.94	F08/FA09	II?	14.334 ± 0.001	13.694 ± 0.001	12.247 ± 0.001	10.980	10.059	8.838 ± 0.004	8.374 ± 0.001	7.958 ± 0.003	7.251 ± 0.004	4.785 ± 0.017
35	054553.544+003308.75	F08/FA09	II	13.727 ± 0.001	13.074 ± 0.001	12.280 ± 0.001	11.666 ± 0.001	10.963 ± 0.001	10.200 ± 0.001	9.857 ± 0.002	9.426 ± 0.003	8.686 ± 0.003	6.002 ± 0.020
36	054703.977+001114.32	F08/FA09	II	13.630 ± 0.001	13.158 ± 0.001	12.304 ± 0.001	11.742 ± 0.001	10.968 ± 0.001	10.074 ± 0.002	9.649 ± 0.002	9.261 ± 0.004	8.349 ± 0.002	5.360 ± 0.012
37	054618.012+001212.28		II?	14.043 ± 0.001	13.944 ± 0.001	12.340 ± 0.001	11.704	10.562	9.714 ± 0.001	9.289 ± 0.002	9.019 ± 0.003	8.622 ± 0.003	6.363 ± 0.016
38	054630.057+001209.61	F08/FA09	II	14.146 ± 0.001	13.310 ± 0.001	12.364 ± 0.001	11.222	10.834 ± 0.001	9.841 ± 0.002	9.521 ± 0.002	9.247 ± 0.004	8.384 ± 0.002	5.434 ± 0.015
39	054620.872+000809.35	F08/FA09	II?	14.295 ± 0.001	13.488 ± 0.001	12.405 ± 0.001	11.619 ± 0.001	10.489	9.922 ± 0.001	9.501 ± 0.002	9.016 ± 0.003	8.081 ± 0.004	4.905 ± 0.016
40	054710.891+003205.96	F08/FA09	II	13.856 ± 0.001	13.238 ± 0.001	12.524 ± 0.002	11.504	11.083 ± 0.002	10.404 ± 0.002	10.035 ± 0.002	9.627 ± 0.003	9.032 ± 0.004	6.768 ± 0.016
41	054652.409+002001.64	F08/FA09	II?	14.208 ± 0.001	13.474 ± 0.001	12.553 ± 0.002	11.451	10.874	9.739 ± 0.001	9.314 ± 0.002	8.962 ± 0.004	8.058 ± 0.014	4.637 ± 0.011
42	054604.774-001416.48		I	17.138 ± 0.005	15.148 ± 0.002	12.664 ± 0.002	11.264 ± 0.001	10.175 ± 0.001	7.222 ± 0.002	6.276 ± 0.002	5.404 ± 0.002	4.419 ± 0.002	0.638 ± 0.007
43	054634.898+000420.75	F08/FA09	II	14.562 ± 0.001	13.619 ± 0.001	12.752 ± 0.002	11.653	11.208 ± 0.002	10.753 ± 0.003	10.605 ± 0.003	10.248 ± 0.021	9.884 ± 0.052	6.904 ± 0.041
44	054647.404+001259.26		II	14.784 ± 0.002	13.934 ± 0.001	12.767 ± 0.002	11.661	11.015 ± 0.002	10.169 ± 0.001	9.742 ± 0.002	9.298 ± 0.004	8.728 ± 0.003	6.644 ± 0.023
45	054726.329+001848.35		II	14.844 ± 0.002	13.812 ± 0.001	12.771 ± 0.002	11.705	11.169 ± 0.002	10.563 ± 0.002	10.345 ± 0.002	10.078 ± 0.007	9.534 ± 0.018	6.990 ± 0.048
46	054703.314+002323.21		II?	15.603 ± 0.002	14.248 ± 0.002	12.774 ± 0.002	11.198	10.461	9.812 ± 0.002	9.553 ± 0.003	9.214 ± 0.004	8.680 ± 0.007	6.651 ± 0.034
47	054553.115-001324.85	F08/FA09	II	13.879 ± 0.001	13.429 ± 0.001	12.791 ± 0.002	12.090 ± 0.002	11.785 ± 0.002	11.362 ± 0.002	11.280 ± 0.003	11.214 ± 0.009	10.942 ± 0.015	6.456 ± 0.025
48	054643.843+001532.29	F08/FA09	II	14.237 ± 0.001	13.670 ± 0.001	12.811 ± 0.002	12.016 ±						

ID	Name/Position (VISTAomsJ)	Previous Identification	Lada 20 Class	Z	Y	J	H	K <sub>S</sub>	IRAC 3.6 $\mu$ m	IRAC 4.5 $\mu$ m	IRAC 5.8 $\mu$ m	IRAC 8 $\mu$ m	MIPS 24 $\mu$ m
49	054616.747+000713.37	FA09	II	15.174 $\pm$ 0.002	13.946 $\pm$ 0.001	12.815 $\pm$ 0.002	11.816 $\pm$ 0.001	11.122 $\pm$ 0.002	10.537 $\pm$ 0.002	10.286 $\pm$ 0.002	10.020 $\pm$ 0.007	9.597 $\pm$ 0.017	6.905 $\pm$ 0.035
50	054628.885+001331.15	FA09	II?	15.418 $\pm$ 0.002	14.371 $\pm$ 0.002	12.859 $\pm$ 0.002	11.392	10.142	9.090 $\pm$ 0.001	8.594 $\pm$ 0.002	8.154 $\pm$ 0.002	7.271 $\pm$ 0.001	4.343 $\pm$ 0.010
51	054716.584-000056.38	F08/FA09	II	14.297 $\pm$ 0.001	13.619 $\pm$ 0.001	12.874 $\pm$ 0.002	12.224 $\pm$ 0.002	11.709 $\pm$ 0.002	11.209 $\pm$ 0.002	10.842 $\pm$ 0.003	10.489 $\pm$ 0.006	9.827 $\pm$ 0.008	7.547 $\pm$ 0.039
52	054653.579+000005.80		Flat?	15.329 $\pm$ 0.002	13.957 $\pm$ 0.001	12.885 $\pm$ 0.002	11.075	10.282	8.791 $\pm$ 0.004	8.182 $\pm$ 0.004	7.626 $\pm$ 0.002	6.630 $\pm$ 0.002	3.318 $\pm$ 0.011
53	054640.768+002722.54	F08/FA09	II	14.642 $\pm$ 0.002	14.010 $\pm$ 0.001	12.893 $\pm$ 0.002	12.245 $\pm$ 0.002	11.400 $\pm$ 0.002	10.274 $\pm$ 0.001	9.866 $\pm$ 0.002	9.524 $\pm$ 0.003	8.877 $\pm$ 0.003	6.366 $\pm$ 0.021
54	054631.566+000640.00		II	15.063 $\pm$ 0.002	14.194 $\pm$ 0.001	12.920 $\pm$ 0.002	11.636	10.995 $\pm$ 0.002	10.260 $\pm$ 0.002	9.899 $\pm$ 0.002	9.520 $\pm$ 0.008	8.854 $\pm$ 0.021	6.441 $\pm$ 0.026
55	054658.032+001427.85	F08/FA09	II	14.563 $\pm$ 0.001	13.697 $\pm$ 0.001	12.932 $\pm$ 0.002	12.079 $\pm$ 0.002	11.536 $\pm$ 0.002	10.658 $\pm$ 0.002	10.264 $\pm$ 0.002	9.778 $\pm$ 0.006	8.985 $\pm$ 0.016	5.922 $\pm$ 0.016
56	054707.925+002024.68		II	14.955 $\pm$ 0.002	13.982 $\pm$ 0.001	12.941 $\pm$ 0.002	11.719	11.149 $\pm$ 0.002	10.489 $\pm$ 0.003	10.128 $\pm$ 0.003	9.628 $\pm$ 0.009	8.727 $\pm$ 0.017	5.801 $\pm$ 0.021
57	054706.169+002032.50	FA09	II?	15.665 $\pm$ 0.002	14.368 $\pm$ 0.002	12.963 $\pm$ 0.002	11.405	10.627	9.724 $\pm$ 0.003	9.243 $\pm$ 0.002	8.719 $\pm$ 0.010	7.862 $\pm$ 0.022	4.479 $\pm$ 0.012
58	054653.769+000034.06		II	15.027 $\pm$ 0.002	13.983 $\pm$ 0.001	12.980 $\pm$ 0.002	12.050 $\pm$ 0.002	11.457 $\pm$ 0.002	10.687 $\pm$ 0.003	10.356 $\pm$ 0.002	10.001 $\pm$ 0.020	9.293 $\pm$ 0.044	6.020 $\pm$ 0.022
59	054706.984+003155.96	F08/FA09	II	14.896 $\pm$ 0.002	13.915 $\pm$ 0.001	13.016 $\pm$ 0.002	11.791	11.271 $\pm$ 0.002	10.137 $\pm$ 0.002	9.502 $\pm$ 0.001	9.107 $\pm$ 0.003	8.079 $\pm$ 0.002	4.694 $\pm$ 0.009
60	054622.987+000426.47	F08/FA09	II	14.756 $\pm$ 0.002	13.925 $\pm$ 0.001	13.048 $\pm$ 0.002	12.082 $\pm$ 0.002	11.544 $\pm$ 0.002	10.786 $\pm$ 0.002	10.398 $\pm$ 0.002	9.940 $\pm$ 0.008	9.182 $\pm$ 0.018	6.336 $\pm$ 0.021
61	054625.882+000931.93	F08/FA09	II	14.417 $\pm$ 0.001	13.800 $\pm$ 0.001	13.058 $\pm$ 0.002	12.248 $\pm$ 0.002	11.734 $\pm$ 0.002	10.847 $\pm$ 0.002	10.373 $\pm$ 0.002	10.120 $\pm$ 0.007	9.382 $\pm$ 0.019	6.639 $\pm$ 0.019
62	054651.478+001921.32	F08/FA09	II	14.682 $\pm$ 0.002	13.883 $\pm$ 0.001	13.132 $\pm$ 0.002	12.284 $\pm$ 0.002	11.802 $\pm$ 0.002	11.232 $\pm$ 0.003	10.929 $\pm$ 0.002	10.638 $\pm$ 0.016	9.664 $\pm$ 0.021	6.333 $\pm$ 0.019
63	054717.162+001824.55	F08/FA09	II	14.745 $\pm$ 0.002	14.143 $\pm$ 0.001	13.150 $\pm$ 0.002	12.105 $\pm$ 0.002	11.246 $\pm$ 0.002	10.065 $\pm$ 0.002	9.537 $\pm$ 0.002	9.249 $\pm$ 0.017	8.725 $\pm$ 0.066	5.977 $\pm$ 0.021
64	054644.837+001659.81	F08/FA09	II	14.879 $\pm$ 0.002	14.033 $\pm$ 0.001	13.169 $\pm$ 0.002	12.135 $\pm$ 0.002	11.626 $\pm$ 0.002	10.999 $\pm$ 0.003	10.818 $\pm$ 0.003	10.655 $\pm$ 0.011	10.091 $\pm$ 0.021	5.872 $\pm$ 0.016
65	054636.105+000626.86	FA09	Flat	16.765 $\pm$ 0.004	15.373 $\pm$ 0.003	13.169 $\pm$ 0.002	11.270	10.373 $\pm$ 0.001	8.409 $\pm$ 0.004	7.935 $\pm$ 0.003	7.459 $\pm$ 0.003	6.201 $\pm$ 0.005	2.434 $\pm$ 0.009
66	054719.186+001920.64		II	14.882 $\pm$ 0.002	14.052 $\pm$ 0.001	13.178 $\pm$ 0.002	12.239 $\pm$ 0.002	11.694 $\pm$ 0.002	10.770 $\pm$ 0.003	10.374 $\pm$ 0.002	9.846 $\pm$ 0.009	8.711 $\pm$ 0.021	5.247 $\pm$ 0.013
67	054638.324+000548.77	FA09	II	16.080 $\pm$ 0.003	14.922 $\pm$ 0.002	13.251 $\pm$ 0.002	12.237 $\pm$ 0.002	11.114 $\pm$ 0.002	9.891 $\pm$ 0.003	9.276 $\pm$ 0.002	8.861 $\pm$ 0.009	7.940 $\pm$ 0.022	4.702 $\pm$ 0.020
68	054638.401+001511.63	FA09	II	15.078 $\pm$ 0.002	14.156 $\pm$ 0.001	13.273 $\pm$ 0.002	12.515 $\pm$ 0.002	11.983 $\pm$ 0.002	11.342 $\pm$ 0.002	11.074 $\pm$ 0.002	10.817 $\pm$ 0.007	10.284 $\pm$ 0.007	7.402 $\pm$ 0.034
69	054637.537+000800.49		II	15.457 $\pm$ 0.002	14.524 $\pm$ 0.002	13.277 $\pm$ 0.002	11.966	11.268 $\pm$ 0.002	10.540 $\pm$ 0.003	10.135 $\pm$ 0.002	9.881 $\pm$ 0.015	9.319 $\pm$ 0.036	6.735 $\pm$ 0.032
70	054629.584+001057.22	FA09	II	15.502 $\pm$ 0.002	14.373 $\pm$ 0.002	13.303 $\pm$ 0.002	12.343 $\pm$ 0.002	11.718 $\pm$ 0.002	10.829 $\pm$ 0.002	10.435 $\pm$ 0.002	9.934 $\pm$ 0.006	9.232 $\pm$ 0.017	6.522 $\pm$ 0.024
71	054653.723+002631.27		II	15.152 $\pm$ 0.002	14.242 $\pm$ 0.002	13.333 $\pm$ 0.002	12.503 $\pm$ 0.002	12.045 $\pm$ 0.002	11.597 $\pm$ 0.002	11.327 $\pm$ 0.003	11.193 $\pm$ 0.008	10.541 $\pm$ 0.011	8.319 $\pm$ 0.061
72	054645.145+000346.44	FA09	II	15.294 $\pm$ 0.002	14.314 $\pm$ 0.002	13.341 $\pm$ 0.002	12.190 $\pm$ 0.002	11.438 $\pm$ 0.002	10.562 $\pm$ 0.005	10.247 $\pm$ 0.005	10.073 $\pm$ 0.034	9.314 $\pm$ 0.094	6.244 $\pm$ 0.031
73	054610.303-000006.70	FA09	II	15.223 $\pm$ 0.002	14.472 $\pm$ 0.002	13.431 $\pm$ 0.002	12.457 $\pm$ 0.002	11.522 $\pm$ 0.002	10.614 $\pm$ 0.002	10.083 $\pm$ 0.002	9.637 $\pm$ 0.004	8.791 $\pm$ 0.008	5.769 $\pm$ 0.013
74	054654.434+002114.18		II	15.995 $\pm$ 0.003	15.132 $\pm$ 0.002	13.434 $\pm$ 0.002	12.668 $\pm$ 0.002	11.550 $\pm$ 0.002	10.734 $\pm$ 0.002	10.315 $\pm$ 0.002	9.938 $\pm$ 0.004	9.341 $\pm$ 0.012	6.592 $\pm$ 0.027
75	054705.301+002310.10		II?	17.542 $\pm$ 0.006	15.822 $\pm$ 0.003	13.473 $\pm$ 0.002	10.786	9.439	7.978 $\pm$ 0.003	7.424 $\pm$ 0.003	6.954 $\pm$ 0.001	6.430 $\pm$ 0.001	3.302 $\pm$ 0.011
76	054651.850+001938.57	FA09	II	15.637 $\pm$ 0.002	14.608 $\pm$ 0.002	13.510 $\pm$ 0.002	12.452 $\pm$ 0.002	11.817 $\pm$ 0.002	11.127 $\pm$ 0.003	10.782 $\pm$ 0.003	10.371 $\pm$ 0.025	9.416 $\pm$ 0.045	5.739 $\pm$ 0.020
77	054632.714+000851.72		II	15.738 $\pm$ 0.003	14.697 $\pm$ 0.002	13.516 $\pm$ 0.002	12.078 $\pm$ 0.002	11.100 $\pm$ 0.002	9.614 $\pm$ 0.002	9.048 $\pm$ 0.001	8.658 $\pm$ 0.003	8.022 $\pm$ 0.006	5.760 $\pm$ 0.018
78	054727.365+000515.29		II	15.992 $\pm$ 0.003	14.697 $\pm$ 0.002	13.521 $\pm$ 0.002	12.219 $\pm$ 0.002	11.380 $\pm$ 0.002	10.105 $\pm$ 0.002	9.470 $\pm$ 0.001	9.002 $\pm$ 0.003	8.358 $\pm$ 0.002	5.646 $\pm$ 0.013
79	054638.566+002206.02	F08/FA09	II	15.568 $\pm$ 0.002	14.422 $\pm$ 0.002	13.588 $\pm$ 0.003	12.260 $\pm$ 0.002	11.840 $\pm$ 0.002	11.137 $\pm$ 0.002	10.842 $\pm$ 0.002	10.502 $\pm$ 0.007	9.853 $\pm$ 0.006	7.673 $\pm$ 0.045
80	054719.722+000121.86	F08/FA09	II	15.240 $\pm$ 0.002	14.330 $\pm$ 0.002	13.632 $\pm$ 0.003	13.060 $\pm$ 0.003	12.648 $\pm$ 0.003	11.737 $\pm$ 0.003	11.158 $\pm$ 0.002	10.785 $\pm$ 0.007	10.168 $\pm$ 0.007	7.102 $\pm$ 0.028
81	054646.961+000709.05		II?	16.576 $\pm$ 0.004	15.162 $\pm$ 0.002	13.641 $\pm$ 0.003	11.960	10.921	9.561 $\pm$ 0.003	8.925 $\pm$ 0.002	8.352 $\pm$ 0.011	7.554 $\pm$ 0.030	4.721 $\pm$ 0.016
82	054557.929+000248.62	F08/FA09	II	15.161 $\pm$ 0.002	14.216 $\pm$ 0.002	13.659 $\pm$ 0.003	12.762 $\pm$ 0.002	12.282 $\pm$ 0.003	11.373 $\pm$ 0.003	11.134 $\pm$ 0.003	10.887 $\pm$ 0.009	10.412 $\pm$ 0.013	7.806 $\pm$ 0.050
83	054604.579+000038.09	F08/FA09	II	15.432 $\pm$ 0.002	14.190 $\pm$ 0.001	13.665 $\pm$ 0.003	12.320 $\pm$ 0.002	12.016 $\pm$ 0.002	11.056 $\pm$ 0.002	10.752 $\pm$ 0.003	10.436 $\pm$ 0.005	9.839 $\pm$ 0.013	6.656 $\pm$ 0.024
84	054710.721+003211.00		II	15.422 $\pm$ 0.002	14.493 $\pm$ 0.002	13.702 $\pm$ 0.003	12.914 $\pm$ 0.002	12.480 $\pm$ 0.003	11.722 $\pm$ 0.003	11.321 $\pm$ 0.004	11.027 $\pm$ 0.008	10.298 $\pm$ 0.012	7.929 $\pm$ 0.044
85	054703.748+002329.29		II	16.828 $\pm$ 0.004	15.300 $\pm$ 0.003	13.714 $\pm$ 0.003	12.007	11.056 $\pm$ 0.002	9.579 $\pm$ 0.002	8.887 $\pm$ 0.002	8.171 $\pm$ 0.002	7.304 $\pm$ 0.002	4.967 $\pm$ 0.010
86	054706.258+002453.96		III?	17.532 $\pm$ 0.006	15.708 $\pm$ 0.003	13.749 $\pm$ 0.003	11.686	10.658	10.059 $\pm$ 0.002	9.990 $\pm$ 0.002	9.811 $\pm$ 0.005	9.759 $\pm$ 0.007	8.786 $\pm$ 0.112
87	054719.904+001613.08	FA09	II	16.064 $\pm$ 0.003	14.926 $\pm$ 0.002	13.759 $\pm$ 0.003	12.650 $\pm$ 0.002	11.958 $\pm$ 0.002	11.153 $\pm$ 0.003	10.699 $\pm$ 0.003	10.234 $\pm$ 0.013	9.550 $\pm$ 0.031	5.741 $\pm$ 0.024
88	054618.598+000707.93	FA09	II	16.374 $\pm$ 0.003	15.183 $\pm$ 0.002	13.772 $\pm$ 0.003	12.382 $\pm$ 0.002	11.352 $\pm$ 0.002	10.311 $\pm$ 0.002	9.801 $\pm$ 0.002	9.151 $\pm$ 0.005	8.469 $\pm$ 0.015	5.453 $\pm$ 0.014
89	054542.794+000101.88	FA09	II	15.203 $\pm$ 0.002	14.463 $\pm$ 0.002	13.796 $\pm$ 0.003	13.215 $\pm$ 0.003	12.830 $\pm$ 0.004	12.084 $\pm$ 0.004	11.732 $\pm$ 0.004	11.390 $\pm$ 0.011	10.662 $\pm$ 0.012	7.692 $\pm$ 0.050
90	054631.712+002508.04	FA09	II	16.249 $\pm$ 0.003	14.980 $\pm$ 0.002	13.812 $\pm$ 0.003	12.357 $\pm$ 0.002	11.663 $\pm$ 0.002	10.839 $\pm$ 0.002	10.506 $\pm$ 0.002	10.148 $\pm$ 0.006	9.471 $\pm$ 0.005	6.477 $\pm$ 0.017
91	054556.728-000025.34	FA09	II	15.521 $\pm$ 0.002	14.736 $\pm$ 0.002	13.831 $\pm$ 0.003	12.852 $\pm$ 0.002	12.347 $\pm$ 0.003	11.884 $\pm$ 0.003	11.483 $\pm$ 0.004	10.978 $\pm$ 0.009	10.109 $\pm$ 0.011	6.096 $\pm$ 0.008

ID	Name/Position (VISTAomsJ)	Previous Identification	Lada Class	Z	Y	J	H	K <sub>S</sub>	IRAC 3.6 $\mu$ m	IRAC 4.5 $\mu$ m	IRAC 5.8 $\mu$ m	IRAC 8 $\mu$ m	MIPS 24 $\mu$ m
104	054637.522+000654.65		II	17.132 $\pm$ 0.005	15.645 $\pm$ 0.003	14.115 $\pm$ 0.003	12.771 $\pm$ 0.002	11.888 $\pm$ 0.002	10.977 $\pm$ 0.003	10.584 $\pm$ 0.002	10.298 $\pm$ 0.022	9.641 $\pm$ 0.044	5.888 $\pm$ 0.021
105	054554.679+002122.28		II	16.257 $\pm$ 0.003	15.034 $\pm$ 0.002	14.134 $\pm$ 0.003	13.329 $\pm$ 0.003	12.777 $\pm$ 0.003	12.023 $\pm$ 0.003	11.692 $\pm$ 0.004	11.342 $\pm$ 0.010	10.680 $\pm$ 0.015	7.651 $\pm$ 0.042
106	054735.166+002129.12		III?	18.753 $\pm$ 0.012	16.581 $\pm$ 0.005	14.136 $\pm$ 0.003	11.695	10.492	9.758 $\pm$ 0.001	9.682 $\pm$ 0.002	9.459 $\pm$ 0.003	9.411 $\pm$ 0.005	8.928 $\pm$ 0.134
107	054645.000+001132.86	FA09	II	16.112 $\pm$ 0.003	15.471 $\pm$ 0.003	14.168 $\pm$ 0.003	13.261 $\pm$ 0.003	12.456 $\pm$ 0.003	11.350 $\pm$ 0.002	10.895 $\pm$ 0.003	10.331 $\pm$ 0.007	9.229 $\pm$ 0.005	5.910 $\pm$ 0.016
108	054652.680+000608.78		Flat	17.103 $\pm$ 0.005	15.737 $\pm$ 0.003	14.299 $\pm$ 0.004	12.819 $\pm$ 0.002	12.019 $\pm$ 0.002	10.992 $\pm$ 0.018	10.569 $\pm$ 0.013	9.661 $\pm$ 0.082	8.156 $\pm$ 0.148	4.190 $\pm$ 0.029
109	054625.915+000709.16		II	17.527 $\pm$ 0.006	15.923 $\pm$ 0.004	14.352 $\pm$ 0.004	12.931 $\pm$ 0.002	11.977 $\pm$ 0.002	11.045 $\pm$ 0.002	10.468 $\pm$ 0.003	10.024 $\pm$ 0.008	9.348 $\pm$ 0.026	6.468 $\pm$ 0.021
110	054609.607+000331.21	FA09	II	16.861 $\pm$ 0.004	15.161 $\pm$ 0.002	14.375 $\pm$ 0.004	12.579 $\pm$ 0.002	12.116 $\pm$ 0.003	10.956 $\pm$ 0.002	10.599 $\pm$ 0.002	10.305 $\pm$ 0.007	9.625 $\pm$ 0.013	6.241 $\pm$ 0.015
111	054648.730+002138.30	FA09	II	17.210 $\pm$ 0.005	15.839 $\pm$ 0.003	14.411 $\pm$ 0.004	13.080 $\pm$ 0.003	12.321 $\pm$ 0.003	11.497 $\pm$ 0.003	11.123 $\pm$ 0.003	10.806 $\pm$ 0.008	10.161 $\pm$ 0.009	7.064 $\pm$ 0.028
112	054713.193+001055.38		II	16.644 $\pm$ 0.004	15.472 $\pm$ 0.003	14.432 $\pm$ 0.004	13.030 $\pm$ 0.003	12.254 $\pm$ 0.003	10.796 $\pm$ 0.003	10.281 $\pm$ 0.002	9.844 $\pm$ 0.004	8.926 $\pm$ 0.003	5.944 $\pm$ 0.019
113	054629.132+000259.06		II?	18.235 $\pm$ 0.009	16.505 $\pm$ 0.005	14.452 $\pm$ 0.004	12.299 $\pm$ 0.002	11.026	9.566 $\pm$ 0.002	8.899 $\pm$ 0.002	8.198 $\pm$ 0.003	7.425 $\pm$ 0.004	4.972 $\pm$ 0.011
114	054702.968+000602.48		II	16.909 $\pm$ 0.004	15.731 $\pm$ 0.003	14.496 $\pm$ 0.004	13.287 $\pm$ 0.003	12.595 $\pm$ 0.003	11.779 $\pm$ 0.003	11.424 $\pm$ 0.004	11.131 $\pm$ 0.018	10.693 $\pm$ 0.045	8.170 $\pm$ 0.082
115	054625.706+002341.32		II?	18.825 $\pm$ 0.012	16.905 $\pm$ 0.006	14.498 $\pm$ 0.004	12.233 $\pm$ 0.002	10.643	8.645 $\pm$ 0.003	7.899 $\pm$ 0.004	7.425 $\pm$ 0.001	6.564 $\pm$ 0.001	3.917 $\pm$ 0.017
116	054612.261+000807.73	FA09	II	16.510 $\pm$ 0.004	15.363 $\pm$ 0.003	14.516 $\pm$ 0.004	13.943 $\pm$ 0.004	13.445 $\pm$ 0.005	12.720 $\pm$ 0.004	12.317 $\pm$ 0.004	11.907 $\pm$ 0.017	11.100 $\pm$ 0.018	8.213 $\pm$ 0.070
117	054612.180+000349.82		II	16.835 $\pm$ 0.004	15.690 $\pm$ 0.003	14.545 $\pm$ 0.004	13.422 $\pm$ 0.003	12.486 $\pm$ 0.003	11.454 $\pm$ 0.003	10.975 $\pm$ 0.003	10.758 $\pm$ 0.012	10.272 $\pm$ 0.034	6.942 $\pm$ 0.031
118	054555.131+001139.48	FA09	II	16.153 $\pm$ 0.003	15.095 $\pm$ 0.002	14.571 $\pm$ 0.004	13.758 $\pm$ 0.004	13.398 $\pm$ 0.005	12.522 $\pm$ 0.004	12.126 $\pm$ 0.005	11.855 $\pm$ 0.014	11.259 $\pm$ 0.019	8.718 $\pm$ 0.093
119	054649.085+002838.32	FA09	II	17.200 $\pm$ 0.005	15.933 $\pm$ 0.004	14.644 $\pm$ 0.004	13.359 $\pm$ 0.003	12.614 $\pm$ 0.003	11.696 $\pm$ 0.003	11.312 $\pm$ 0.003	10.916 $\pm$ 0.009	10.210 $\pm$ 0.007	7.679 $\pm$ 0.039
120	054633.309+002255.49		II	18.008 $\pm$ 0.008	16.407 $\pm$ 0.005	14.664 $\pm$ 0.004	12.958 $\pm$ 0.003	12.044 $\pm$ 0.002	11.219 $\pm$ 0.003	10.854 $\pm$ 0.003	10.311 $\pm$ 0.006	9.666 $\pm$ 0.005	6.537 $\pm$ 0.017
121	054549.558+000838.80	FA09	II	16.361 $\pm$ 0.003	15.540 $\pm$ 0.003	14.674 $\pm$ 0.004	13.947 $\pm$ 0.004	13.382 $\pm$ 0.005	12.745 $\pm$ 0.004	12.232 $\pm$ 0.004	11.921 $\pm$ 0.016	11.228 $\pm$ 0.017	8.621 $\pm$ 0.081
122	054704.358+002319.82		II	17.943 $\pm$ 0.007	16.370 $\pm$ 0.005	14.679 $\pm$ 0.004	12.864 $\pm$ 0.002	11.805 $\pm$ 0.002	10.508 $\pm$ 0.003	9.938 $\pm$ 0.003	9.443 $\pm$ 0.004	8.788 $\pm$ 0.006	5.710 $\pm$ 0.026
123	054708.710+001634.79	FA09	Flat	17.218 $\pm$ 0.005	15.926 $\pm$ 0.004	14.777 $\pm$ 0.004	13.528 $\pm$ 0.003	12.790 $\pm$ 0.004	11.954 $\pm$ 0.008	11.595 $\pm$ 0.005	11.279 $\pm$ 0.052	10.290 $\pm$ 0.086	5.412 $\pm$ 0.039
124	054640.878+002329.04		II	19.028 $\pm$ 0.014	17.170 $\pm$ 0.008	15.023 $\pm$ 0.005	12.823 $\pm$ 0.002	11.520 $\pm$ 0.002	10.526 $\pm$ 0.001	9.956 $\pm$ 0.002	9.823 $\pm$ 0.003	9.412 $\pm$ 0.004	6.348 $\pm$ 0.015
125	054712.458+002215.28		II	19.202 $\pm$ 0.015	17.244 $\pm$ 0.008	15.210 $\pm$ 0.005	13.146 $\pm$ 0.003	12.103 $\pm$ 0.003	11.141 $\pm$ 0.005	10.736 $\pm$ 0.003	10.293 $\pm$ 0.009	9.562 $\pm$ 0.024	6.209 $\pm$ 0.017
126	054701.068+002543.82		II	17.878 $\pm$ 0.007	16.502 $\pm$ 0.005	15.282 $\pm$ 0.006	14.224 $\pm$ 0.005	13.560 $\pm$ 0.005	12.741 $\pm$ 0.008	11.684 $\pm$ 0.013	11.761 $\pm$ 0.025	11.443 $\pm$ 0.042	8.531 $\pm$ 0.082
127	054727.751+002035.74		II?	21.042 $\pm$ 0.056	18.422 $\pm$ 0.019	15.286 $\pm$ 0.006	12.037 $\pm$ 0.002	9.530	8.296 $\pm$ 0.003	7.471 $\pm$ 0.003	6.771 $\pm$ 0.001	5.972 $\pm$ 0.003	3.690 $\pm$ 0.014
128	054702.076+002329.76		II	18.915 $\pm$ 0.013	17.004 $\pm$ 0.007	15.432 $\pm$ 0.006	13.759 $\pm$ 0.004	12.876 $\pm$ 0.004	11.707 $\pm$ 0.003	11.146 $\pm$ 0.003	10.778 $\pm$ 0.009	10.186 $\pm$ 0.013	7.647 $\pm$ 0.050
129	054607.861+001001.78		I	17.842 $\pm$ 0.007	16.833 $\pm$ 0.006	15.451 $\pm$ 0.006	13.671 $\pm$ 0.004	12.062 $\pm$ 0.002	9.926 $\pm$ 0.004	8.596 $\pm$ 0.003	7.632 $\pm$ 0.002	6.622 $\pm$ 0.003	2.123 $\pm$ 0.029
130	054727.036+001926.54		II	19.739 $\pm$ 0.021	17.745 $\pm$ 0.011	15.492 $\pm$ 0.006	13.077 $\pm$ 0.003	11.739 $\pm$ 0.002	10.330 $\pm$ 0.002	9.762 $\pm$ 0.002	9.313 $\pm$ 0.004	8.571 $\pm$ 0.003	6.050 $\pm$ 0.019
131	054726.098+001927.91		Flat	20.298 $\pm$ 0.032	17.927 $\pm$ 0.013	15.782 $\pm$ 0.007	13.134 $\pm$ 0.003	11.699 $\pm$ 0.002	9.600 $\pm$ 0.001	8.962 $\pm$ 0.001	8.335 $\pm$ 0.002	7.642 $\pm$ 0.003	4.396 $\pm$ 0.010
132	054607.209+001323.12		I	18.078 $\pm$ 0.008	16.992 $\pm$ 0.007	15.800 $\pm$ 0.007	14.492 $\pm$ 0.005	13.473 $\pm$ 0.005	11.653 $\pm$ 0.012	10.475 $\pm$ 0.014	10.009 $\pm$ 0.018	9.496 $\pm$ 0.020	4.444 $\pm$ 0.018
133	054720.792+001924.49		Flat	18.798 $\pm$ 0.012	17.252 $\pm$ 0.008	15.822 $\pm$ 0.008	13.761 $\pm$ 0.004	12.425 $\pm$ 0.003	10.171 $\pm$ 0.002	9.396 $\pm$ 0.002	8.895 $\pm$ 0.006	8.218 $\pm$ 0.015	5.022 $\pm$ 0.018
134	054714.885+002118.83		II	19.878 $\pm$ 0.024	17.951 $\pm$ 0.013	15.948 $\pm$ 0.008	14.238 $\pm$ 0.005	13.144 $\pm$ 0.004	12.148 $\pm$ 0.004	11.741 $\pm$ 0.004	11.392 $\pm$ 0.024	10.697 $\pm$ 0.058	8.221 $\pm$ 0.082
135	054640.148+001038.93		II	19.945 $\pm$ 0.025	17.862 $\pm$ 0.013	15.972 $\pm$ 0.008	14.323 $\pm$ 0.005	13.306 $\pm$ 0.004	12.268 $\pm$ 0.004	11.852 $\pm$ 0.003	11.375 $\pm$ 0.017	10.528 $\pm$ 0.021	7.029 $\pm$ 0.041
136	054700.852+000512.16		II	20.004 $\pm$ 0.026	17.970 $\pm$ 0.014	16.125 $\pm$ 0.009	14.576 $\pm$ 0.006	13.459 $\pm$ 0.005	12.196 $\pm$ 0.004	11.648 $\pm$ 0.004	11.150 $\pm$ 0.026	10.458 $\pm$ 0.079	7.011 $\pm$ 0.035
137	054648.543+002128.19	FA09	Flat	18.378 $\pm$ 0.009	17.939 $\pm$ 0.013	16.297 $\pm$ 0.010	15.167 $\pm$ 0.008	13.565 $\pm$ 0.005	12.059 $\pm$ 0.004	11.252 $\pm$ 0.003	10.552 $\pm$ 0.008	9.443 $\pm$ 0.005	5.559 $\pm$ 0.015
138	054657.125+002535.69		II	20.783 $\pm$ 0.046	18.588 $\pm$ 0.022	16.321 $\pm$ 0.010	14.274 $\pm$ 0.005	13.030 $\pm$ 0.004	11.859 $\pm$ 0.003	11.268 $\pm$ 0.003	10.893 $\pm$ 0.007	9.973 $\pm$ 0.008	6.957 $\pm$ 0.034
139	054613.008+000814.78	FA09	I	17.848 $\pm$ 0.007	17.144 $\pm$ 0.007	16.412 $\pm$ 0.011	15.592 $\pm$ 0.010	15.158 $\pm$ 0.014	14.321 $\pm$ 0.013	13.589 $\pm$ 0.010	12.728 $\pm$ 0.034	10.900 $\pm$ 0.019	6.318 $\pm$ 0.024
140	054627.338+000851.86		Flat	18.175 $\pm$ 0.008	17.428 $\pm$ 0.009	16.539 $\pm$ 0.011	15.554 $\pm$ 0.010	14.485 $\pm$ 0.009	12.879 $\pm$ 0.008	12.204 $\pm$ 0.006	11.425 $\pm$ 0.031	10.332 $\pm$ 0.051	6.625 $\pm$ 0.027
141	054722.908+002058.09		Flat	20.397 $\pm$ 0.034	18.610 $\pm$ 0.022	16.608 $\pm$ 0.012	14.857 $\pm$ 0.007	13.974 $\pm$ 0.006	12.418 $\pm$ 0.007	11.568 $\pm$ 0.005	10.934 $\pm$ 0.014	10.018 $\pm$ 0.022	6.431 $\pm$ 0.024
142	054651.401+001947.14	FA09	I	18.887 $\pm$ 0.013	17.887 $\pm$ 0.013	16.707 $\pm$ 0.013	15.375 $\pm$ 0.009	14.389 $\pm$ 0.008	12.461 $\pm$ 0.006	11.340 $\pm$ 0.004	10.459 $\pm$ 0.015	9.123 $\pm$ 0.036	5.507 $\pm$ 0.012
143	054659.028+002457.96		II	22.205 $\pm$ 0.150	19.863 $\pm$ 0.066	16.708 $\pm$ 0.013	14.028 $\pm$ 0.004	12.216 $\pm$ 0.003	10.827 $\pm$ 0.001	10.133 $\pm$ 0.002	9.872 $\pm$ 0.003	9.417 $\pm$ 0.005	6.800 $\pm$ 0.033
144	054725.398+001939.86		Flat	21.237 $\pm$ 0.066	19.252 $\pm$ 0.039	16.718 $\pm$ 0.013	14.474 $\pm$ 0.005	12.727 $\pm$ 0.003	10.961 $\pm$ 0.002	10.122 $\pm$ 0.002	9.398 $\pm$ 0.004	8.519 $\pm$ 0.005	5.873 $\pm$ 0.020
145	054745.324+000010.01		II	18.886 $\pm$ 0.013	17.850 $\pm$ 0.012	17.037 $\pm$ 0.015	15.810 $\pm$ 0.012	15.126 $\pm$ 0.013	13.990 $\pm$ 0.007	13.294 $\pm$ 0.008	12.583 $\pm$ 0.022	11.603 $\pm$ 0.022	8.886 $\pm$ 0.113
146	054715.492+001845.97		Flat	—	20.591 $\pm$ 0.126	17.078 $\pm$ 0.016	13.019 $\pm$ 0.003	10.685 $\pm$ 0.001	8.402 $\pm$				

ID	Name/Position (VISTAomsJ)	Previous Identification	Lada Class	$S$	$Z$	$Y$	$J$	$H$	$K_S$	IRAC $3.6\mu\text{m}$	IRAC $4.5\mu\text{m}$	IRAC $5.8\mu\text{m}$	IRAC $8\mu\text{m}$	MIPS $24\mu\text{m}$
159	054603.633-001449.38		I	—	—	$20.854 \pm 0.159$	$18.483 \pm 0.043$	$15.268 \pm 0.008$	$12.807 \pm 0.004$	$9.318 \pm 0.004$	$7.616 \pm 0.003$	$6.454 \pm 0.001$	$5.145 \pm 0.002$	$1.544 \pm 0.011$
160	054637.863-001858.21		Flat	$21.030 \pm 0.056$	$20.046 \pm 0.077$	$18.702 \pm 0.051$	$17.390 \pm 0.038$	$16.025 \pm 0.025$	$14.696 \pm 0.014$	$13.614 \pm 0.012$	$12.394 \pm 0.021$	$11.190 \pm 0.020$	$8.085 \pm 0.082$	$8.085 \pm 0.082$
161	054743.464-002617.88		Flat?	$19.684 \pm 0.021$	$19.193 \pm 0.037$	$18.707 \pm 0.051$	$17.971 \pm 0.061$	$17.202 \pm 0.080$	$15.137 \pm 0.028$	$14.230 \pm 0.015$	$13.404 \pm 0.081$	$12.413 \pm 0.041$	$8.894 \pm 0.153$	$8.894 \pm 0.153$
162	054802.016+001533.44		Flat	$19.951 \pm 0.025$	$19.547 \pm 0.050$	$18.913 \pm 0.061$	$18.392 \pm 0.088$	$17.559 \pm 0.090$	$15.871 \pm 0.027$	$14.690 \pm 0.023$	$13.837 \pm 0.051$	$12.582 \pm 0.046$	$9.375 \pm 0.160$	$9.375 \pm 0.160$
163	054652.639+002208.69		Flat	—	—	—	$18.996 \pm 0.065$	$15.976 \pm 0.013$	$14.143 \pm 0.007$	$12.639 \pm 0.005$	$12.031 \pm 0.004$	$11.422 \pm 0.014$	$10.294 \pm 0.016$	$6.699 \pm 0.020$
164	054608.472-001040.04		I	—	—	$20.209 \pm 0.089$	$19.082 \pm 0.070$	$17.257 \pm 0.034$	$15.301 \pm 0.015$	$12.312 \pm 0.006$	$10.647 \pm 0.003$	$9.388 \pm 0.003$	$8.311 \pm 0.003$	$3.594 \pm 0.008$
165	054655.102+002334.55		I	—	—	—	$19.239 \pm 0.080$	$16.254 \pm 0.016$	$14.326 \pm 0.008$	$11.733 \pm 0.004$	$10.293 \pm 0.002$	$9.213 \pm 0.003$	$8.434 \pm 0.003$	$3.510 \pm 0.008$
166	054619.435+003544.45		I	$20.751 \pm 0.045$	$19.798 \pm 0.062$	$19.281 \pm 0.082$	$18.265 \pm 0.079$	$17.306 \pm 0.072$	$15.024 \pm 0.018$	$14.101 \pm 0.017$	$13.183 \pm 0.034$	$12.160 \pm 0.038$	$8.569 \pm 0.086$	$8.569 \pm 0.086$
167	054731.686+002020.65		Flat	—	—	—	$19.541 \pm 0.103$	$16.221 \pm 0.016$	$14.070 \pm 0.007$	$12.091 \pm 0.010$	$11.184 \pm 0.011$	$10.433 \pm 0.007$	$9.463 \pm 0.006$	$5.787 \pm 0.020$
168	054627.303-002140.75		I	$20.845 \pm 0.048$	$20.566 \pm 0.123$	$19.597 \pm 0.108$	$18.536 \pm 0.100$	$17.915 \pm 0.123$	$16.220 \pm 0.039$	$15.158 \pm 0.039$	$14.084 \pm 0.096$	$13.260 \pm 0.096$	$9.352 \pm 0.151$	$9.352 \pm 0.151$
169	054533.825+003936.76		I	$20.546 \pm 0.038$	$20.079 \pm 0.080$	$19.922 \pm 0.143$	$18.917 \pm 0.140$	$17.925 \pm 0.124$	$15.722 \pm 0.032$	$14.906 \pm 0.028$	$13.858 \pm 0.081$	$13.102 \pm 0.067$	$9.515 \pm 0.203$	$9.515 \pm 0.203$
170	054550.636+000629.88		Flat	$20.827 \pm 0.047$	$20.191 \pm 0.088$	$19.956 \pm 0.147$	$18.992 \pm 0.149$	$18.203 \pm 0.160$	$16.090 \pm 0.031$	$15.291 \pm 0.034$	$14.386 \pm 0.104$	$13.155 \pm 0.080$	$9.989 \pm 0.267$	$9.989 \pm 0.267$
171	054621.758+003708.15		I	$21.186 \pm 0.063$	$20.651 \pm 0.133$	$19.989 \pm 0.151$	$19.088 \pm 0.163$	$18.170 \pm 0.155$	$16.456 \pm 0.052$	$15.736 \pm 0.044$	$14.442 \pm 0.140$	$13.500 \pm 0.083$	$9.496 \pm 0.178$	$9.496 \pm 0.178$
172	054613.517-000855.75		Flat	—	—	—	$20.067 \pm 0.162$	$16.249 \pm 0.016$	$13.700 \pm 0.006$	$11.708 \pm 0.003$	$11.036 \pm 0.003$	$10.549 \pm 0.007$	$9.531 \pm 0.005$	$5.725 \pm 0.018$
173	054700.403+002259.34		Flat	—	—	—	$20.820 \pm 0.317$	$18.128 \pm 0.070$	$16.101 \pm 0.027$	$14.131 \pm 0.010$	$13.390 \pm 0.011$	$12.656 \pm 0.037$	$11.807 \pm 0.075$	$8.080 \pm 0.079$
174	054751.834+001553.14		I	$22.870 \pm 0.269$	—	—	$20.824 \pm 0.318$	$19.407 \pm 0.217$	$18.432 \pm 0.196$	$16.504 \pm 0.058$	$15.694 \pm 0.067$	$14.609 \pm 0.174$	$13.176 \pm 0.086$	$9.937 \pm 0.253$
175	054552.811+002722.86		I?	$22.832 \pm 0.260$	$21.475 \pm 0.280$	—	—	$19.585 \pm 0.254$	$18.675 \pm 0.220$	$16.729 \pm 0.058$	$15.661 \pm 0.050$	$14.460 \pm 0.107$	$13.397 \pm 0.084$	$10.002 \pm 0.277$
176	054607.227-001134.91		II	—	—	—	—	$18.051 \pm 0.066$	$13.949 \pm 0.006$	$11.262 \pm 0.003$	$10.358 \pm 0.002$	$9.929 \pm 0.005$	$9.789 \pm 0.006$	$8.484 \pm 0.083$
177	054630.635-000235.41		I	—	—	—	—	$19.340 \pm 0.204$	$15.550 \pm 0.018$	$13.934 \pm 0.012$	$10.867 \pm 0.003$	$10.851 \pm 0.012$	$10.592 \pm 0.020$	$6.773 \pm 0.021$
178	054633.159+000001.94		I	—	—	—	—	$16.377 \pm 0.017$	$13.893 \pm 0.006$	$10.936 \pm 0.004$	$9.897 \pm 0.002$	$9.401 \pm 0.010$	$8.722 \pm 0.026$	$2.433 \pm 0.003$
179	054647.014+000027.25		I	—	—	—	—	$17.934 \pm 0.059$	$15.520 \pm 0.018$	$12.641 \pm 0.045$	$11.324 \pm 0.025$	$10.727 \pm 0.053$	$10.173 \pm 0.051$	$3.655 \pm 0.018$
180	054637.553+000033.88		I	—	—	—	—	$19.079 \pm 0.162$	$15.587 \pm 0.018$	$12.581 \pm 0.005$	$10.582 \pm 0.003$	$9.022 \pm 0.004$	$7.638 \pm 0.005$	$2.806 \pm 0.006$
181	054627.237+000149.80		I	—	—	—	—	$18.253 \pm 0.078$	$14.656 \pm 0.010$	$11.737 \pm 0.003$	$10.729 \pm 0.003$	$10.053 \pm 0.008$	$9.460 \pm 0.028$	$6.099 \pm 0.018$
182	054704.006+002210.34		I	—	—	—	—	$15.867 \pm 0.012$	$12.262 \pm 0.003$	$8.546 \pm 0.004$	$6.705 \pm 0.002$	$5.745 \pm 0.003$	$4.623 \pm 0.001$	$0.712 \pm 0.035$
183	054613.568+002349.16		Flat	—	—	—	—	$16.365 \pm 0.017$	$13.634 \pm 0.005$	$11.743 \pm 0.003$	$11.104 \pm 0.003$	$10.691 \pm 0.008$	$10.357 \pm 0.007$	$6.559 \pm 0.022$
184	054555.417+002436.07		Flat	—	—	—	—	$19.176 \pm 0.176$	$18.078 \pm 0.143$	$16.165 \pm 0.040$	$15.103 \pm 0.034$	$14.120 \pm 0.087$	$13.403 \pm 0.113$	$9.839 \pm 0.247$
185	054657.967+002501.88		I	—	—	—	—	$19.768 \pm 0.300$	$17.253 \pm 0.069$	$15.336 \pm 0.018$	$14.393 \pm 0.018$	$13.621 \pm 0.054$	$12.412 \pm 0.038$	$8.375 \pm 0.083$
186	054630.754+003100.77		Flat	—	—	—	—	$19.222 \pm 0.184$	$17.991 \pm 0.132$	$15.961 \pm 0.039$	$15.387 \pm 0.039$	$13.998 \pm 0.093$	$13.588 \pm 0.121$	$9.717 \pm 0.212$